# Chapter 3
# Optical and electrical characteristics of a PECVD-grown MOS diode with buried Si nanocrystal

## 3.1 Introduction

Nanocrystallite Si structures that exhibit quantum confinement effect have led to the development of novel Si-based functional devices such as light emitting diodes, resonant tunneling diode and single-electron transistor, etc. [1-3] In particular, most investigations on preparing silicon oxide or nitride with buried Si nanocrystals (nc-Si) in matrices have been performed using plasma-enhanced chemical vapor deposition (PECVD), in which pure monosilane ($SiH_4$) and nitrous oxide ($N_2O$) or ammonia ($NH_3$) are decomposed at high plasma power from 100 to 450 W. [4, 5] The PECVD deposition associated with subsequent heat treatment enables the easy deposition of a Si-rich $SiO_x$ film with a sufficiently high density of excess Si atoms by controlling the fluence of reactive gases. However, there are few studies on the correlation between the $N_2O/SiH_4$ fluence ratio and the substrate temperature for optimum nc-Si precipitation. Moreover, few studies have addressed the deposition of Si-rich $SiO_2$ ($SiO_x$) using low-plasma-power PECVD methods. In this work, the near-infrared continuous-wave (CW) and time-resolved (TR) PL spectroscopes are employed to study the effects of the substrate temperature and $N_2O/SiH_4$ fluent ratio on the PL intensity and lifetime of PECVD-grown, thermally annealed Si-rich SiOx film with buried nc-Si. The synthesis of the $SiO_x$ film by suppressing oxygen decomposition in a low plasma power PECVD at high substrate temperature was

investigated. The effects of chamber pressure, $SiH_4/N_2O$ fluence ratio and plasma power on the excess Si ratio are characterized. The morphology and density of synthesized nc-Si is monitored by high-resolution transmission electron microscopy (HRTEM). In particular, the separation of Si and $SiO_2$ phases, the formation of nc-Si, and their transition to the crystalline phase were investigated using the electron energy loss spectroscopy (EELS). The evolution of the electroluminescence (EL) of a metal-oxide-semiconductor light emitting diode (MOSLED) that was fabricated on the PECVD-grown and nc-Si embedded $SiO_x$ at a high deposition temperature and threshold plasma power is also obtained.

# 3.2 PECVD-grown Si-rich $SiO_2$ film deposited at high-plasma power, different fluence ratios and substrate temperatures

## 3.2.1 Sample preparation and experimental setup

Si-rich $SiO_x$ films with a thickness of about 100 nm were deposited on (100)-oriented *n*-type Si substrates with resistivity of 4-7 Ω·cm using a conventional high-density PECVD system at a pressure and a forward radio frequency (RF) power of 50 mTorr and 200 W, respectively. The samples were prepared at different gas mixtures and substrate temperatures. Gas mixtures with a constant $SiH_4$ flucence of 30 sccm and various $N_2O$ flucences (from 90 to 180 sccm) were used. The substrate temperature was changed from 100 to 350 $^{o}$C. The detailed processing conditions are shown in Table 1. The Si-rich $SiO_x$ samples were encapsulated by annealing in a quartz furnace with $N_2$ atmosphere at 1100 $^{o}$C from 1 to 5 h to induce precipitation of nc-Si. The thickness of a Si-rich $SiO_x$ sample containing nc-Si structures was

determined by $\alpha$-step measurement after etching. Room-temperature CWPL measurement with a pumping source, a He-Cd laser, at a wavelength and an average power intensity of 325 nm and 5 $W/cm^2$, respectively, was carried out with a photon-counting system, which includes a fluorescence spectrophotometer (Jobin Yvon, TRIAX-320) with a wavelength resolution of 0.06 nm and a photomultiplier (Jobin Yvon, Model 1424M). In a TRPL experiment, a $SiO_x$ film was pumped using a Q-switched YAG laser (Continuum, NY 60) at 355 nm and a repetition rate of 1 Hz. The pumping pulse width and pulse energy were 60 ps and 0.5 mJ, respectively. A PL signal was detected using a single-grating monochromator with a near-infrared photomultiplier tube and recorded using a sampling scope (Lecroy, Model LT372 with a resolution of 2 ns). [6]

### 3.2.2 Effect of $N_2O/SiH_4$ ratio on density of nc-Si in PECVD-grown Si-rich $SiO_x$ film

After a Si-rich $SiO_x$ film PECVD-grown at a constant substrate temperature of 100 $^oC$, a constant $SiH_4$ fluence of 30 sccm, and a $N_2O/SiH_4$ ratio of 4 was annealed at 1100 $^oC$ for 3 h, a maximum PL intensity at a wavelength of 728 nm was observed (Fig. 1). An optimum $N_2O$ fluence was found at 120 sccm, as shown in the inset of Fig. 1. The excess Si density of the PECVD-grown Si-rich $SiO_x$ film is proportional to the density of nc-Si and the $SiH_4$ fluence. However, as the $N_2O/SiH_4$ ratio increases from 4 to 6, the density of nc-Si buried in the PECVD-grown Si-rich $SiO_x$ film decreases and the PL intensity at 400-700 nm increases. The effects of the $N_2O/SiH_4$ ratio and the evolution of radiative centers buried in the $SiO_x$ structure are seldom addressed. A sufficient amount of oxygen atoms, generated from the $N_2O$ gas, completely reacts with Si atoms, generated from the $SiH_4$ gas, to deposit a

stoichiometric $SiO_2$ film. After thermal annealing, oxygen-related defects, such as a neutral oxygen vacancy defect [7-9] (NOV, denoted as $O_3\equiv$Si-Si$\equiv O_3$), are activated. In a previous study, [7] NOV defects attributed to the displacement of oxygen atoms from the stoichiometric $SiO_2$ matrix by the bombardment of Si ions, were usually observed in a Si-ion-implanted Si-rich $SiO_2$ film. In our experiment, the enhanced PL intensity at the wavelength of 455 nm is attributed to the NOV defect in the $SiO_2$ matrix fabricated using a sufficient $N_2O$ fluence ($N_2O/SiH_4$ ratios $>5$). This indicates that the growth of the stoichiometric $SiO_2$ matrix at high $N_2O/SiH_4$ ratios is preferred. On the other hand, for the samples with $N_2O/SiH_4$ ratios of 5 or larger, the PL intensity at a wavelength of 750 nm is not enhanced, since a complete reaction with oxygen and Si atoms causes few excess Si atoms to hardly precipitate nc-Si.

A low PL intensity of around 750 nm was obtained for the sample fabricated with a $N_2O/SiH_4$ ratio $<4$. The size of nc-Si buried in the Si-rich $SiO_x$ film depends on the density of oxygen atoms in the Si-rich $SiO_x$ film. Nc-Si larger than 5 nm can be observed in the Si-rich $SiO_x$ film prepared with small $N_2O$ fluences ($N_2O/SiH_4$ ratios $<4$). In addition, the small $N_2O/SiH_4$ ratio cannot produce the stoichiometric $SiO_2$ matrix due to the insufficient density of oxygen atoms. It induces an imperfect quantum confinement effect in the $SiO_2$ matrix, resulting in the suppression of the PL radiating from nc-Si. The PL intensities at 455 nm for the NOV defect and 750 nm for nc-Si in the sample prepared with a $N_2O/SiH_4$ ratio of 3 are observed to be lower than those of the sample prepared with a $N_2O/SiH_4$ ratio of 4. As shown in Fig. 1, the enhanced PL intensity in the visible range, attributed to oxygen-related defects, and the highest PL intensity in the near-infrared range, attributed to nc-Si, was observed in the sample with the $N_2O/SiH_4$ ratio of 4.

This indicates that at a suitable $N_2O/SiH_4$ ratio, not only the highest density of excess Si atoms, resulting in a large amount of nc-Si, but also the stoichiometric $SiO_2$

matrix, resulting in a better quantum confinement between nc-Si and the $SiO_2$ matrix, can be obtained. Therefore, the $N_2O/SiH_4$ ratio should be well controlled.

### 3.2.3 Effect of substrate temperature on density of excess Si atoms and nc-Si

In general, a stoichiometric $SiO_2$ film is grown using a PECVD system at a substrate temperature and an RF power of 350-400 $^oC$ and 700-900 W, respectively. However, a nearly stoichiometric $SiO_2$ film can be grown at an RF power as low as 200 W in our case. Typically, a further reduction in either substrate temperature or RF power results in an evident phase separation between Si and $SiO_2$ during deposition. The two different methods are potentially applicable to the fabrication of a Si-rich $SiO_x$ film with a high excess Si density. Previously, the substrate temperature was maintained at 350~400 $^oC$, and the RF power was decreased to <50 W for preparing a Si-rich $SiO_x$ film. [2,3] Nonetheless, the effect of reducing the substrate temperature at a given RF power on the excess Si density of the PECVD-grown Si-rich $SiO_x$ film was seldom discussed. By increasing the substrate temperature from 100 to 350 $^oC$, the PL spectra of Si-rich $SiO_x$ films PECVD-grown at an RF power of 200 W are shown in Fig. 2. The peak PL intensity shows a distinct decreasing trend with increasing substrate temperature. The near-infrared PL is mainly due to the quantum confinement effect of the nc-Si cluster, whereas the defect-related visible PL can hardly be obtained in the PECVD-grown Si-rich $SiO_x$ film.

After annealing, Ma *et al*. also observed the Si nanoparticles embedded in a Si-rich $SiO_2$ film deposited at a substrate temperature between 30 and 450 $^oC$. [10] The highest density of nc-Si was found in the Si-rich $SiO_2$ film deposited at a low

substrate temperature of 30 $^{o}$C, which was attributed to the enhanced phase separation between Si and $SiO_2$ during low-substrate-temperature deposition at a high RF power in the PECVD chamber. [11] Obviously, a low-substrate-temperature deposition that facilitates the generation of nonstoichiometric $SiO_2$ was revealed in our experiment. The slightly increasing PL at 455 nm in the Si-rich $SiO_x$ film deposited at such a low substrate temperature was also observed due to dense oxygen-related NOV defects. Thus, a low substrate temperature is required for depositing a $SiO_x$ film with a high excess Si density when the RF power of the PECVD system used is high. The peak PL at a wavelength between 703 and 728 nm is contributed by nc-Si with a diameter ranging between 3.5 and 3.8 nm. A nearly stoichiometric $SiO_2$ matrix prevents the formation of a large-size precipitate of mobile Si atoms, which increases the density of small-size nc-Si. Under a high RF power condition, a high substrate temperature is detrimental to the formation of nc-Si, since it favors stoichiometric $SiO_2$ deposition.

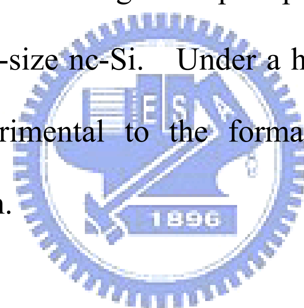

### 3.2.4 Effect of annealing time on size and PL lifetime of nc-Si

The annealing-time-dependent PL spectra of sample A7 with the highest density of excess Si atoms are shown in Fig. 3. The optimum annealing time for the precipitation of nc-Si is 3 h, corresponding to the peak wavelength of 703 nm. The PL at a wavelength of 455 nm for the as-grown sample A7 is attributed to the NOV defect. After annealing at 1100 $^{o}$C for 1 h, the sample A7 has the maximum PL intensity of the NOV defect. In comparison, the optimized annealing time for the PECVD-grown $SiO_x$ sample is similar to that (1.5 h) for the multienergy Si-ion-implanted $SiO_2$ sample reported previously.[12-14] Moreover, the NOV

intensities of both the PECVD-grown and Si-ion-implanted $SiO_2$ samples decrease after annealing at 1100 $^{o}$C for 2 h. As the annealing time increases to 5 h, the peak intensity of the NOV defect rapidly decreases since most of the NOV defects are annealed in a high-temperature environment. In addition, the peak wavelength is redshifted from 455 to 727 nm due to the precipitation of nc-Si, as shown in Fig. 4. This indicates that the increase in PL intensity at a wavelength of 600 nm is attributed to small-size nc-Si. After 1-h annealing, the excess Si atoms rapidly precipitate into small-size nc-Si. Moreover, nc-Si is enlarged due to the accumulation of small-size nc-Si after a long thermal annealing time of up to 3 h. An obvious redshift of the peak PL wavelength is also found after annealing times of 1 to 3 h. However, as the annealing time increases to 5 h, a small redshift is observed due to large-size nc-Si. On the other hand, the variations in the PL intensities of NOV and nc-Si as a function of annealing time are shown in Fig. 4. The intensities of nc-Si were determined at a wavelength of 703 nm. The optimized annealing time for nc-Si is 3 h and the intensity of nc-Si decreases by a factor of 5 as the annealing time increases to 5 h due to the reaction of nc-Si with mobile oxygen atoms resulting in the regrowth of $SiO_2$ matrix.

The PL lifetimes of sample A7 for the annealing times of 1, 2, and 3 h are 27, 39, and 43 μs, respectively, and the PL decayed spectra are shown in Fig. 5. The calculated size of nc-Si buried in the Si-rich $SiO_x$ film grown under the conditions of sample A7 is around 3.7 nm. In comparison, Brongersma *et al*. [8] formed Si nanocrystals (diameter, 2-5 nm) by Si ion implantation and thermal annealing at 1100 $^{o}$C, and the room-temperature lifetime of Si nanocrystals with a PL wavelength of about 710 nm is similar to our result. Moreover, the decayed lifetime of nc-Si embedded in the sample A7 after annealing for 3 h ($\tau_{nc\text{-}si}$=43 μs ) is very close to that obtained from the plot (lifetime $\tau$ vs $\lambda_{PL}$) given by Garcia *et al*. [15]

### 3.2.5 Conclusion

In conclusion, the CWPL and TRPL properties of thermally annealed PECVD-grown nc-Si samples that show luminescence in the near-infrared spectrum are studied. The optimum annealing time at a temperature of 1100 $^{o}$C and the $N_2O/SiH_4$ ratio are 3 h and 4, respectively. The optimum processing substrate temperature is determined to be 100 $^{o}$C according to the substrate-temperature-dependent spectra. As the $N_2O/SiH_4$ ratio <4, the size of nc-Si buried in the Si-rich $SiO_x$ film depends on the density of oxygen atoms in the Si-rich $SiO_x$ film, and the low $N_2O/SiH_4$ ratio causes an imperfect quantum confinement effect in the $SiO_2$ matrix, resulting in the suppression of the PL radiating from nc-Si. At a $N_2O/SiH_4$ ratio >4, the intensity between 700 and 800 nm is much weak because a sufficient amount of oxygen atoms completely reacts with silicon atoms to generate a $SiO_2$ film, and the amount of excess Si is too low to precipitate nc-Si. The normalized TRPL traces of samples with an optimum $N_2O/SiH_4$ ratio and an optimum processing substrate temperature, after annealing at 1100 $^{o}$C for 1, 2, and 3 h are 27, 39, and 43 μs, respectively. The number of excess Si atoms in such a non-stoichiometric $SiO_x$ matrix is increasing markedly with temperature at substrate temperatures as low as 30-100$^{o}$C because of the enhanced phase separation between Si and $SiO_2$ during low-substrate-temperature deposition. In other words, a normal PECVD growth condition at high RF power and high substrate temperature for the stoichiometric $SiO_2$ deposition is detrimental to the synthesis of nc-Si. However, high RF power inevitably contributes to plasma treatment on the substrate surface, which may severely worsen the electrical performance of nearby CMOS devices and circuitry. A low-plasma-power PECVD synthesis of $SiO_x$ film is therefore necessary to prevent possible damage, which was seldom discussed in previous investigations.

## 3.3 Deposition temperature dependent electrical characteristics of low-plasma-power PECVD deposited electroluminescent silicon-rich silicon oxide film

### 3.3.1 Sample preparation and experimental setup

The plasma power was set as low as 40 W, and the $SiO_x$ films were grown on p-type Si (100) substrate using a PECVD system with different $SiH_4/N_2O$ fluence ratios, chamber pressures and substrate temperatures. The $SiH_4$ fluence remained at 20 sccm, whereas the $N_2O$ fluence varied from 105 to 130 sccm. After deposition, the samples were annealed in a quartz furnace with flowing $N_2$ at 1100°C for 15-180 min. The room-temperature PL of the $SiO_x$ films, pumped by an Nd:YAG laser at a wavelength and an average intensity of 532 nm and 61 W/cm$^2$, respectively, was analyzed using a fluorescence spectrophotometer (CVI, DK240 with resolution of 0.06 nm) and a photomultiplier (Hamamatsu, Model R928). To characterize the orientation and size of nc-Si, the bright-field cross-section image was taken using HRTEM (JEOL 4000EX) with a primary electron energy of 400 keV and a point-to-point resolution of 0.18 nm. In the TRPL experiment, the $SiO_x$ samples were pumped by a third-harmonic-generated YAG laser (NY 60, Continuum) at 355 nm. The repetition rate, the full width of the pulse at half maximum (FWHM), and the average power of the YAG laser are 1 Hz, 60 ps and 0.5 mJ/pulse, respectively. The TRPL signal was detected by a time-correlated single-photon counting system and the nc-Si dependent luminescent lifetime was determined using Einstein's two-level quantized radiation model. [16] The PL intensity of nc-Si can be approximated by $I = \eta\sigma\phi(t)N/\tau$, where $\sigma$ is the absorption cross-section of nc-Si that can be determined theoretically using $\sigma = \lambda^2/8\pi\Delta\nu\tau$ (where $\lambda$ and $\Delta\nu$ are the peak wavelength and the linewidth of the PL spectrum), [17,18] $\eta$ is a relative coefficient, $\tau$ is the lifetime of nc-Si, $\phi(t)$ is the pumping flux, and $N$ is the nc-Si concentration. [19]

### 3.3.2 Effect of $N_2O/SiH_4$ ratio on density of nc-Si in PECVD-grown $SiO_x$ film

Varying the $N_2O/SiH_4$ fluence ratio controls the Si composition in the deposited $SiO_x$, which strongly influences the size and density of the nc-Si after annealing. [20, 21] In particular, the optimal annealing condition could also be changed for the $SiO_x$ grown at different $N_2O/SiH_4$ fluence ratios. Controlling $SiH_4$ fluence does not yield a predictable result as the decomposition rate of Si is well beyond that of the oxygen under such conditions. In this case, $N_2O$ fluence dominates the low-plasma-power PECVD growth. The optimal annealing times for $SiO_x$ samples prepared under different $N_2O$ fluences are tentatively varied, which is attributed to the evolutional thermal conductivity of the $SiO_x$ caused by the variation in the density of excess Si atoms in the $SiO_x$ film prepared under different $N_2O$ fluences. After furnace annealing at 1100$^o$C for 60 min, the highest PL intensity and the largest peak wavelength among these samples were observed from the sample that was prepared at the an $N_2O$ fluence of 120 sccm, as shown in Fig. 6. The highest excess Si condition was observed in the $SiO_x$ sample that was prepared at an $N_2O$ fluence of 120 sccm. As the $N_2O$ fluence increased from 105 to 120 sccm, the PL intensity doubled. However, the PL intensity decreased by a factor of three, as the $N_2O$ fluence was increased further to 130 sccm. The peak PL wavelength concurrently increased from 733 to 754.5 nm as the $N_2O$ fluence increased from 105 to 120 sccm, and then decreased to 690 nm as the $N_2O$ fluence increased to 130 sccm or higher. Increasing the $N_2O$ fluence leads to the adsorption of more oxygen atoms on the substrate, improving oxidation and contributing to the smaller size of nc-Si, which in turn blue-shifts the PL peak after annealing. Both the size and density of nc-Si then decrease. In contrast, insufficient oxygen atoms were decomposed at $N_2O$ fluences

of under 120 sccm, yielding dense Si atoms and contributing to the larger size of nc-Si with smaller density after annealing. In addition to the observation of decreasing PL intensity, the less decreasing trend of PL wavelength correlates closely with the almost constant size of nc-Si.

As the annealing time increases from 15 to 60 min, the lifetimes of the nc-Si in $SiO_x$ films decrease from 52 to 20 μs, as shown in Fig. 7 and Table 2. A stretched exponential function: $I(t) = I_0 \exp(-t/\tau)$, was used to fit the data, in which τ is an effective decay time. The luminescent lifetime increases from 20 to 52 μs as the nc-Si size extends from 4.0 to 4.2 nm. Moreover, the nc-Si lifetime increases smoothly with the increment of the nc-Si size, as determined by Garcia et al. [22] The theoretical carrier-transition equation can be simplified to $I_{PL} \propto \sigma\phi(t) \, {}^{1}\!/_{\tau_{PL}} N_{nc-Si}$, [22, 23] and the variation of the nc-Si density can be estimated by the PL intensity ($I_{PL}$) and the lifetime ($\tau_{PL}$) of nc-Si, where $\sigma$ and $\phi(t)$ are the emission (absorption) cross-section of nc-Si and the pumping photon flux density obtained from the pumping power, respectively. The product of these two terms for different annealing-time samples is a constant. As the annealing time increases from 15 to 60 min, the density of nc-Si is decreases from $8.3\times10^{18}$ $cm^{-3}$ to $1.2\times10^{18}$ $cm^{-3}$, which variation correlates closely with the evolution of measured PL, as reported by Augustine et al. [23] In principle, a longer annealing time essentially produces larger size and less dense nc-Si because of the accumulation of small-size nc-Si and the unchanged density of Si atoms in the PECVD-grown $SiO_x$ sample. The planar-view HRTEM image of the PECVD-grown $SiO_x$ sample that was annealed for 15 min reveals that the average diameter of nc-Si is about 4.2 nm, as shown in Fig. 8. The full-width at half maximum of the size distribution of the nc-Si embedded in the $SiO_x$ film is estimated to be ±1.4 nm, as shown in Fig. 9. The estimated volume

density of the nc-Si buried in the 15 min-annealed PECVD-grown $SiO_x$ film is about $8.3 \times 10^{18}$ $cm^{-3}$. In our experiment, the PL intensity of PECVD-grown $SiO_x$ samples was the largest in the sample that was annealed for 15 min (see Fig. 10). When the annealing time gradually increases to 60 min, the excessive thermal energy causes the re-growth of the $SiO_2$ matrix as well as the re-oxidation of nc-Si. This fact can be proved by the slightly blue-shift of the PL as the annealing time increases and the intensity decreases. It also is highly consistent with the result of the carrier rate equations. Indeed, the PL peak wavelengths exhibit a blue-shift from 760 to 742 nm, which correlates well with the decrease in the size of the nc-Si. Theoretically, the dominant size of nc-Si decreases from 4.5 to 4.2 nm and the width of the size distribution of nc-Si increases as annealing duration lengthens from 15 to 60 min, according to the Delerue's equation [22, 24] of $E(\lambda) = 1.12 + (3.73/ d^{1.39})$, where $E(\lambda)$ is the wavelength-related energy and d is the size of nc-Si. Furthermore, the spectral linewidth of PL spectra ($\Delta\lambda$) increases from 137 to 187 nm, which also corroborates the increase in the width of the size distribution ($\Delta d$) from $\pm 1.4$ nm to $\pm 1.7$ nm, as shown in Fig. 11.

On the other hand, the maximum PL intensities of 60 min-annealed samples prepared under different chamber pressures between 40 and 70 mtorr increase with the annealing time, as shown in Fig. 12. At a $SiH_4/N_2O$ fluence ratio of 1:6, the optimal chamber pressure for the PECVD-grown $SiO_x$ sample with the highest PL intensity is 60 mtorr, as presented in the inset of Fig. 12. The PL intensity decreases as the process pressure decreases less than 60 mtorr. The presence of insufficient reactants at a process pressure of under 60 mtorr contributed to the lower excess Si ion density and the difficulty of precipitating nc-Si.

### 3.3.3 Effect of substrate temperature on density of nc-Si

In EELS analysis, the primary electron that is incident into the standard Si matrix with covalent Si≡Si bonds loses energy because of the versatile up-transitions of the inner shell electrons at the 2s and 2p orbits of the Si atom. Typically, $L_{2,3}$ denotes the transition of electrons at $2P_{1/2}$ and $2P_{3/2}$ orbits, and $L_1$ denotes that for electrons at $2S_{1/2}$ in Si. These interactions contribute to the relative peak observed at different energy losses of the EELS spectrum, in which the first peak corresponds to the up-transition of electrons from the $2P_{1/2}$ or $2p_{3/2}$ level to the vacuum. The lose of kinetic energy of the primary electron that is caused by a Si-$L_{2,3}$ transition in a standard Si substrate is about 101 eV, as shown in Fig. 13. Alternatively, the Si-$L_{2,3}$ transition in a standard $SiO_2$ consumes more of the energy of the primary electron, shifting the corresponding EELS peak to 110 eV with a full-width-at-half-maximum (FWHM) of 4.1 eV. In the PECVD-grown $SiO_x$ sample, the spectral linewidth is broadened to 7.7 eV as the stoichiometric condition of the $SiO_x$ deviates from that of the $SiO_2$. The EELS intensity of the Si-$L_{2,3}$ transition in PECVD-grown $SiO_x$ sample is much lower than that of standard $SiO_2$ since the PECVD-grown $SiO_x$ film is amorphous phase. After 30 min of furnace-annealing, the lose of the kinetic energy of the primary electron that is due to the Si-$L_{2,3}$ transition in the annealed-$SiO_x$ sample decreases to 106 eV. Moreover, the EELS intensity at a kinetic energy loss of 101 eV in the 30 min-annealed sample is two orders of magnitude larger than that in the PECVD-grown $SiO_x$ film, which is attributed to the formation of nc-Si. The excess Si atoms precipitate into nc-Si in the PECVD-grown $SiO_x$ sample and the lower kinetic energy loss of a Si-$L_{2,3}$ transition in crystallite Si cause the combined kinetic energy loss of a Si-$L_{2,3}$ transition in an annealed $SiO_x$ sample with nc-Si to be

significantly lower than that in a PECVD-grown $SiO_x$ sample without nc-Si. Therefore, the formation of nc-Si can be verified by comparing the EELS spectra of the Si substrate, the as-PECVD-grown $SiO_x$ film and the furnace-annealed $SiO_x$ film, since the kinetic energy loss of a Si-$L_{2,3}$ transition varies with the chemical structure.

After furnace annealing at 1100°C for 60 min, the PL spectra of samples that are deposited at various substrate temperatures exhibit an nc-Si dependent broad spectrum between 670 and 850 nm with a slightly broad FWHM linewidth from 101 to 106 nm as the substrate temperature increases from 200 to 400°C, as shown in Fig. 14. The PL peak wavelengths of the samples that are deposited at substrate temperatures of 200, 300, 350 and 400°C shift from 732 nm to 754 nm, as shown in the inset of Fig. 14, which corresponds to the increase in the size of nc-Si and the increase in the density of the excess Si atom. The normalized PL intensity of the sample deposited at a substrate temperature of 400°C is six times higher than that of the sample deposited at 200°C. At low process power (near the threshold plasma power), reactants such as $SiH_4$ and $N_2O$ are hardly dissociated. Since the dissociation energies of the $SiH_4$ and $N_2O$ molecules are 75.6 kcal/mol and 101.5 kcal/mol, [25, 26] respectively, the $N_2O$ molecule is less easily dissociated than the $SiH_4$ molecule resulting in the deposition of excess Si atoms and contributing to the higher density of nc-Si. Furthermore, the weight of a Si atom exceeds those of oxygen and hydrogen atoms, facilitating the deposition of Si atoms. Wong et al. [27] have also demonstrated the deposition of the carbon-doped hydrogenated silicon oxide film using PECVD at substrate temperatures from 200°C to 400°C, and found that the quantity of the Si–O stretching bond decreases as the deposition temperature increases, based on Fourier transform infrared spectroscopy measurements. This result is attributed to the deposition of a few oxygen atoms and the introduction of -CH and

-$CH_3$ groups during the process at a high substrate temperature.

The increase of the peak intensities in the electroluminescent spectra of conventional ITO/$SiO_x$:nc-Si/p-Si/Al MOSLEDs at various substrate temperatures from 200 to 400$^oC$ is well correlated with the evolution of the intensity in the PL spectra, as shown in Fig. 15. The EL intensity of the sample at a substrate temperature of 200$^oC$ is very low since the density of nc-Si is low. At lower substrate temperatures, oxygen atoms are easily adsorbed onto the substrate and hardly diffuse into free space. Therefore, the density of oxygen atoms in the PECVD-grown $SiO_x$ film that is prepared at low substrate temperature exceeds that of such a film prepared at a high substrate temperature. The aforementioned reaction on the substrate contributes to the formation of a stoichiometric $SiO_2$ matrix. After furnace annealing at 1100$^oC$ for 60 min, sufficient oxygen atoms react with excess Si atoms to form the $SiO_2$ matrix. Therefore, the sample that is prepared at a substrate temperature of 200$^oC$ prefer to form a stoichiometric $SiO_2$ matrix and does not precipitate nc-Si, corresponding to a small EL intensity at wavelength of 455 nm and the much lower EL intensity at the near-infrared range. The wavelength of 455 nm is attributed to the emission of the neutral oxygen vacancy (NOV) defect. The low EL intensity at 455 nm also reveals that a few of NOV defects exist in the PECVD-grown $SiO_x$ film that is prepared at a substrate temperature of 200$^oC$, which is like a stoichiometric $SiO_2$ matrix. After the substrate temperature is increased to 300$^oC$, oxygen atoms more easily diffuse into free space than at a substrate temperature of 200$^oC$. The density of excess Si atoms in PECVD-grown $SiO_x$ film increases and fewer oxygen atoms react with excess Si atoms. Since the excess Si atoms are too few, small nc-Si will be precipitated in the PECVD-grown $SiO_x$ film, corresponding to the peak EL wavelength at ~600 nm. Quantum confinement effect

contributes to the increase in the energy of the emission as the size of nc-Si decreases. Briefly, the luminescence at a wavelength of 455 nm for the sample that is prepared at a substrate temperature of 200°C is attributed to the emission from NOV defects, however, the luminescence at 600 nm from the sample prepared at a substrate temperature of 300°C is attributed to the emission from small nc-Si.

For the sample that is prepared at a substrate temperature of 350°C, EL reveals a broaden spectrum between 400 and 850 nm with a peak wavelength of 700 nm and a FWHM spectral linewidth of 338 nm. The peak wavelength red-shifts from 600 to 700 nm as the temperature is increased from 300 to 350°C, revealing the increase in the size of the buried nc-Si. At a low process power and a higher substrate temperature, fewer oxygen atoms are dissociated from molecular $N_2O$ and oxygen atoms cannot easily remain on the substrate, increasing the density of excess Si atoms in the PECVD-grown $SiO_x$ film. The EL intensity at 700 nm of the sample prepared at a substrate temperature of 350°C is more than one order of magnitude higher than that of the sample prepared at 300°C, indicating an increase in the densities of nc-Si and excess Si atoms. During deposition at 350°C, oxygen atoms abruptly leave the substrate, facilitating the deposition of Si atoms. Moreover, FWHM spectral linewidth of 338 nm for the sample prepared at 350°C is much larger than that of 140 nm for the sample prepared at 300°C, indicating that the size distribution in the 350°C sample is wider and that more excess Si atoms are embedded in the PECVD-grown $SiO_x$ film. Increasing the substrate temperature to 400°C reduces the density of the oxygen atoms and increases the density of excess Si atoms, increasing the nc-Si density and the luminescent efficiency. The EL spectrum of the sample that is prepared at a substrate temperature of 400°C reveals a broadening linewidth from 500 to 850 nm, and a peak wavelength of 618 nm with a shrunk FWHM spectral linewidth

of 296 nm, which are both attributed to the emission of nc-Si. However, an EL spectrum with a peak wavelength of ~450 nm was clearly observed from PECVD-grown $SiO_x$ film, which is attributed to the luminescence of the oxygen-related NOV defect. At the high substrate temperature, excess oxygen atoms are seldom adsorbed onto the substrate. After annealing at high temperature, insufficient oxygen atoms can react with Si atom and contribute to oxygen vacancies. The luminescence from NOV defects in PECVD-grown $SiO_x$ film at high substrate temperature reveals the deficiency of oxygen atoms during the formation of nc-Si. This result differs from that obtained for the sample that was prepared at a substrate temperature of 200$^o$C.

At a bias current of 52 μA, ITO/$SiO_x$:nc-Si/p-Si/Al MOSLEDs prepared at substrate temperatures of 300, 350 and 400$^o$C demonstrate red-color emission, which is attributed to the luminescence of nc-Si, as shown in Fig. 16. Since the density of nc-Si embedded is lowest in the sample that was prepared at a substrate temperature of 300$^o$C, the EL pattern of the 300$^o$C-sample demonstrates the darkest emission. The optical power was highest in the sample that was prepared at a substrate temperature of 400$^o$C. As the substrate temperature increases, the optical power of ITO/$SiO_x$:nc-Si/p-Si/Al MOSLED also increases and the device becomes brighter. In other word, the high substrate temperature facilitates the out-diffusion of oxygen atoms and the increase in the number of excess Si atoms in the $SiO_x$ film, contributing to the precipitation of nc-Si and increasing the density of nc-Si. However, unanticipated visible EL components at 455 nm associated with the oxygen vacancy defects are also observed. At a given same bias current, the increasing EL power confirms the increase in the densities of excess Si atoms and nc-Si with the deposition temperature during PECVD growth. After annealing for 60 min, the current-voltage

(I-V) and power-current (P-I) responses of the forward-biased ITO/$SiO_x$:nc-Si/p-Si/Al diode with the buried nc-Si are characterized, as shown in Fig 17. The threshold voltages of the ITO/$SiO_x$:nc-Si/p-Si/Al prepared at 300, 350 and 400$^o$C are 49, 46 and 44 V, respectively. A maximum output power of 47 nW, associated with a P-I slope of 0.84 mW/A, is obtained. According to the Fowler-Nordheim (FN) plot, a clear linear line reveals that the electron transition is the FN tunneling mechanism. [28] To realize the carrier transport behavior in the ITO/$SiO_x$:nc-Si/p-Si/Al MOSLED, the electric field ($E$) dependent emission current density ($J$) is plotted and shown in Fig. 18. A linear $\log(J_G/E^2)$ vs. $1/E$ relationship is observed and well fitted by Fowler-Nordheim (FN) tunneling mechanism. The enhanced conductivity from ITO contact to nc-Si and electron-hole recombination in the nc-Si at beyond FN tunneling threshold are obtained as compared to extremely low leakage observed at low electric fields. Lu *et al.* [29] have demonstrated that the FN tunneling predominates the carrier injection through the nc-Si contained layers separated by thin $SiO_2$ in a MOS diode structure. Without nc-Si, the tunneling current obtained from the pure $SiO_2$ sample is much lower than that from the PECVD-grown $SiO_x$ sample. The threshold electric field to initiate FN tunneling is decreased from 2 to 1.4 MV/cm as the deposition temperature increases from 300 to 400$^o$C, indicating a reduction of the evaluated effective potential barrier height from 2.14±0.01 to 1.1±0.02 eV with the increasing nc-Si density. The P-I slopes of the ITO/$SiO_x$:nc-Si/p-Si/Al MOSLEDs are 0.84, 0.58 and 0.14 mW/A at substrate temperatures of 400, 350, and 300$^o$C. The enlarged P-I slope reveals a higher density of luminescent centers, corresponding to the evolution of the PL and EL spectra. The internal quantum efficiency increases from $5.48\times10^{-5}$ to $5\times10^{-4}$ with a slope of $3.66\times10^{-6}$ /$^o$C as the substrate temperature increases from 300 to 400$^o$C, as plotted in Fig. 19. The external quantum efficiency increases from $2.27\times10^{-6}$ to $1.6\times10^{-5}$. The almost linear increase in the internal

quantum efficiency reveals that the density of nc-Si dominates the energy transition in ITO/$SiO_x$:nc-Si/p-Si/Al MOSLED, since the variation of substrate temperatures causes the density of excess Si atoms and the formation of the nc-Si.

### 3.3.4 Conclusion

In conclusion, the enhanced electroluminescence and external quantum efficiency of metal-$SiO_x$-Si MOSLEDs that are fabricated on nc-Si embedded $SiO_x$ PECVD-grown at high substrate temperature and threshold plasma power are demonstrated. The formation of nc-Si, and the associated structural transition were investigated using EELS. The ratio of $SiH_4$ and $N_2O$ fluences, the process pressure and the substrate temperature used in the fabrication are 1:6, 60 mtorr and 400$^oC$, respectively. Since the dissociation energies of the molecular $SiH_4$ and molecular $N_2O$ are 75.6 kcal/mol and 101.5 kcal/mol, respectively, molecular $N_2O$ dissociates less easily than molecular $SiH_4$ resulting in the deposition excess Si atoms and increasing the density of nc-Si. The threshold voltages of the ITO/$SiO_x$:nc-Si/p-Si/Al that was prepared at 300, 350 and 400$^oC$ are 49, 46 and 44 V, respectively. The maximum output power of 47 nW, associated with a P-I slope of 0.84 mW/A is determined. The internal quantum efficiency increases from $5.48\times10^{-5}$ to $5\times10^{-4}$ with a slope of $3.66\times10^{-6}$ /$^oC$. The external quantum efficiency increases from $2.27\times10^{-6}$ to $1.6\times10^{-5}$.

## 3.4 Carrier transport mechanism of MOS diode

Four carrier transport models were considered as the possible mechanisms in a general metal-oxide-semiconductor (MOS) diode, which include the direct tunneling, the Fowler-Nordheim tunneling, the thermionic emission and the Poole-Frenkel tunneling processes.

### 3.4.1 Directing tunneling

When the applied voltage on a MOS diode is smaller than the barrier height of the metal-oxide interface, the electrons have to penetrate through whole oxide and the gate current is due to direct tunneling in this case, as shown in Fig. 20. Direct tunneling process will not be involved in a MOS diode with relatively thick oxide film (>> 5 nm). The current density of the direct tunneling is given by the expression [30, 31]

$$J_{dir} = \frac{AE_{ox}^2}{\left[1-\sqrt{1-qV_{ox}/\Phi_B}\right]^2} \exp\left(\frac{-B\left[1-\left(1-qV_{ox}/\Phi_B\right)^{1.5}\right]}{E_{ox}}\right), \quad (3\text{-}1)$$

$$A = \frac{q^3\left(m/m_{ox}\right)}{8\pi h\Phi_B} = 1.54\times10^{-6}\frac{\left(m/m_{ox}\right)}{\Phi_B}[\frac{A}{V^2}], \quad (3\text{-}2)$$

$$B = \frac{8\pi\sqrt{2m_{ox}\Phi_B^3}}{3qh} = 6.83\times10^7\sqrt{\left(m_{ox}/m\right)\Phi_B^3}[\frac{V}{cm}], \quad (3\text{-}3)$$

where q is the electron charge, h is Planck's constant, $E_{ox}$ is the applied electric field on the oxide, $m_{ox}$ is the effective electron mass in oxide, m is the free electron mass, $\Phi_B$ is the barrier height and $V_{ox}$ is the voltage applied on the oxide. A simulated direct tunneling current with $m_{ox}/m$ ratio of 0.26, the barrier height of 3.8, the oxide thickness of 2.3 nm and the applied bias from 0 to 3.8 V is shown in Fig. 21, which is much larger than the currents from three different ITO/$SiO_x$:nc-Si/p-Si/Al MOSLEDs

with their $SiO_x$ grown at 300, 350 and 400°C. In our samples, the thicknesses of $SiO_x$ films grown at 300, 350 and 400°C are 270, 230 and 200 nm, respectively. It is impossible to observe the direct tunneling in our samples with the oxide thickness of much larger than 5 nm, since a simulated direct tunneling current with an oxide thickness of 230 nm is zero. The direct tunneling mechanism does not dominate the transport current in the ITO/$SiO_x$:nc-Si/ p-Si/Al MOSLEDs.

### 3.4.2 Fowler-Nordheim tunneling:

When the applied voltage on the MOSLED is equivalent to or larger than the barrier height of the metal-oxide interface, the electrons in the metal side could also penetrate through such a high-electric-field induced triangular barrier, and the gate current can be attributed to the Fowler-Nordheim (F-N) tunneling process, as shown in Fig. 22. Fowler-Nordheim tunneling is the flow of electrons through a triangular potential barrier at high voltages with a current density of $J_{FN}$ given by [32]

$$J_{FN} = \frac{q^3 \left(m/m_{ox}\right)}{8\pi h \Phi_B} E_{ox}^2 \exp\left(\frac{-8\pi\sqrt{2m_{ox}\Phi_B^3}}{3qhE_{ox}}\right), \tag{3-4}$$

where q is the electron charge, h is Planck's constant, $m_{ox}$ is the effective electron mass in the oxide, m is the free electron mass, and $\Phi_B$ is the barrier height. The electric field ($E$) dependent emission current density ($J$) is plotted and fitted in Fig. 18 to realize the carrier transport behavior in the ITO/$SiO_x$:nc-Si/p-Si/Al MOSLED. As a result, the linear relationship is observed in the $\log(J_G/E^2)$ vs. $1/E$ and is well fitted by using the F-N tunneling mechanism expressed in Eq. (3-4). Therefore, our experimental results suggest that the F-N tunneling process is dominant in the ITO/$SiO_x$:nc-Si/ p-Si/Al MOSLEDs with their $SiO_x$ grown at 300, 350 and 400°C.

## 3.4.3 Thermionic emission

If we further consider the current density flowing through a metal-semiconductor contact is dominated by the thermionic emission, as shown in Fig. 23, [33] which can be described as

$$J_{thermionic} = A^{*}T^{2}\exp\left(\frac{-q\Phi_{B}}{kT}\right)\left(\exp\left(\frac{qV}{kT}\right)-1\right), \tag{3-5}$$

where $A^{*}$ = 4 $pqk^{2}m^{*}/h^{3}$ = 120 ($m^{*}/m$), $A/\ cm^{2}\ K^{2}$ is Richardson's constant, m is free electron mass, $m^{*}$ is the effective electron mass, and T is the absolute temperature. A simulated thermionic current with $m^{*}/m$ = 0.26, T = 300 K, and $\Phi_B$ = 3.8 eV is shown in Fig. 24, which is much larger than the currents obtained from three ITO/$SiO_x$:nc-Si/ p-Si/Al MOSLEDs with their $SiO_x$ grown at 300, 350 and 400°C. It is hard to observe the thermionic emission process in such an ITO/$SiO_x$:nc-Si/ p-Si/Al MOSLED.

## 3.4.4 Poole-Frenkel tunneling

If we consider the oxide defect dependent Poole-Frenkel (PF) transport, as shown in Fig. 25, the current density can be evaluated by the following expression: [34, 35]

$$J_{PF}(E_{ox},T) = qN_{t}E_{ox}\mu\exp\left(-\frac{\Phi_{PF}}{kT}\right)\exp\left(\frac{q}{kT}\sqrt{\frac{qE_{ox}}{\pi\varepsilon_{ox}}}\right), \tag{3-6}$$

where $q$ is the electric charge, $E_{ox}$ is the applied electric field, $N_t$ is the volume density of occupied traps, μ is the carrier mobility, $\Phi_{PF}$ is the hopping barrier height and $\varepsilon_{ox}$ is the permittivity of the $SiO_x$ film. Except for this factor, the Schottky emission and the Poole-Frenkel transport exhibit similar electric-field and temperature dependencies. The example of a simulated Poole Frankel tunneling current of the ITO/$SiO_x$:nc-Si/p-Si/Al MOSLEDs with a $SiO_x$ grown at 350°C is shown in Fig. 26,

in which the quoted characteristic parameters are $q$ of $1.6022\times10^{-19}$ C, $N_t$ of $6.4\times10^{18}$ cm$^{-3}$, μ of 20 cm$^2$/V-sec at 300 K, [36] $kT$ of 0.02586 eV at 300 K, $\Phi_{PF}$ of 1.37 eV, and $\varepsilon_{ox}$ of 3.24 for our 350$^o$C-grown sample. As a result, the simulated Poole Frankel tunneling current for the ITO/$SiO_x$:nc-Si/p-Si/Al MOSLED is much lower than the current obtained in our experiments, which clearly indicates the contribution of Fowler-Nordheim tunneling process is more pronounced than that of the Poole-Frenkel tunneling mechanism.

## 3.5 Localized $CO_2$ laser annealing induced dehydrogenation/ablation and optical refinement of silicon-rich silicon dioxide film with embedded Si nanocrystals

### 3.5.1 Introduction

The researching interests in all Si-based light-emitting diodes (LEDs) and integrated-circuits (ICs) have recently been stimulated due to the observation of light emission and optical gain [37] in plasma enhanced chemical vapor deposition (PECVD) grown silicon-rich silicon dioxide ($SiO_x$, $x<2$) films containing the Si nanocrystals (nc-Si). Typically, the synthesis of Si nanocrystal embedded in the Si ion-implanted or PECVD grown $SiO_x$ film requires a long-term and high-temperature furnace annealing process (longer than 30 min) [38]. This approach meets the difficulty in its compatibility with current IC fabricating procedure, in which a high temperature over 500$^o$C may not be applicable and could seriously damage the ICs integrated with $SiO_x$ based LEDs. Furthermore, the conventional annealing methods are not applicable for annealing a prescribed area on the $SiO_x$ film with μm scale.

More recently, the laser based zone annealing approach has successfully utilized in crystallization of $PbZrO_3$ or $PbTiO_3$ material [39] and NiTi shape memory thin films [40]. It is know that the laser annealing techniques can be employed to modify the morphology or structural properties of different materials including metallic thin films [40-42], and dielectrics [43] etc. Nonetheless, the demonstration on the synthesis of Si nanocrystal embedded in the $SiO_x$ film using $CO_2$ laser annealing process that overcomes the aforementioned problems has yet not been reported.

In the room temperature, the real (n) and imaginary (k) parts of the refractive index of $SiO_2$ film at 10.6 μm are approximately 2.224 and 0.102, respectively [44]. Based on the relatively large absorption coefficient of $SiO_2$ material at 10.6 μm, we investigate the structural and optical properties of $CO_2$ laser annealed, PECVD-grown $SiO_x$ film on quartz substrates. The surface temperature simulation using the thermo-physical model for the duration of $CO_2$ laser annealing and the Rutherford Backscattering Spectrometry (RBS) analysis of the $SiO_x$ film are performed. The structural aspects, the luminescent and optical properties, the size and density of Si nanocrystals precipitated in the $CO_2$ laser annealed $SiO_x$ film are analyzed using high resolution transmission electron microscopy (HRTEM), the photoluminescence (PL), the transmission and reflection spectroscopy. The $CO_2$ laser annealing induced dehydrogenation, ablation, and the refinement effects in $SiO_x$ film are also characterized and elucidated.

## 3.5.2 Sample preparation and experimental setup

A $SiO_x$ film was grown on the double-side polished quartz substrate (GE, Type 219) using PECVD at a chamber pressure of 120 mtorr and a $N_2O/SiH_4$ fluence ratio of 6 under induced coupling plasma power of 45 W [45]. The $N_2O$ fluence was

controlled at 120 sccm. The quartz substrate temperature was hold at 150$^o$C for 15 min to balance the substrate temperature and chamber temperature before deposition [46]. After deposition, a continuous-wave $CO_2$ laser (LTT Corp., ILS-II with a maximum power of 30 W) was used to perform the $CO_2$ laser annealing process in atmosphere and $CO_2$ laser intensities were ranging from 1.5 to 13.5 kW/cm$^2$. The $CO_2$ laser annealing time was set as 1 ms. The ablation thickness of $SiO_x$ films was measured using a $\alpha$-step profiler or an atomic force microscope with a depth resolution of 1 nm. PL of the $CO_2$ laser treated $SiO_x$ film was excited by a HeCd laser at laser intensity ($P_{laser}$) of 5 W/cm$^2$ at 325 nm and was analyzed using a monochromator (Jobin Yvon, TRIAX-320) and a photomultiplier (Hamamatsu, R928). Diameters of the beam spot of the excitation laser and $CO_2$ laser are about 30 $\mu$m and 500 $\mu$m, respectively. The spot size of the excitation laser is set to be far smaller than that of the $CO_2$ laser for obtaining PL data from the Laser annealed region with acceptable resolution. During the PL measurement, the excitation laser beam spot was always focused at the center of the $CO_2$ annealed $SiO_x$ film. The transmittance and reflectance of $SiO_x$ films were measured over the wavelength range between 190 and 850 nm (with 0.1 nm resolution) using a commercial UV-VIS transmission and reflection spectrophotometer (Shimadzu, UV-2401PC). The wavelength accuracy of PL system was confirmed using an 850-nm laser diode. An HRTEM (JEOL, 4000EX TEM) with a point-to-point resolution of 0.17 nm was used to characterize the orientation, the lattice spacing, the size, and the density of Si nanocrystals precipitated in the $SiO_x$ film. Ruthford back-scattering (RBS) analysis at a detecting angle of 170$^o$ under 2 MeV $He^+$-ion bombardment and a commercial software of “Ramp” were used to analyze the composition of the $SiO_x$ film.

### 3.5.3 Optical properties and structural diagnosis of $CO_2$ laser-annealed PECVD grown Si-rich $SiO_2$

A precise control on the output power of the $CO_2$ laser results in a fine adjustment on the annealing temperature of the $SiO_x$ film. A $CO_2$ laser annealing process acquires annealing time of only 1 ms for precipitating Si nanocrystals, which is shorter than that required in a furnace-annealing process. The $CO_2$ laser beam can be tightly focused into a spot size of ~10 μm, which is position-controlled using a programmable X-Y translation stage. Therefore, advantages of the $CO_2$ laser based rapid-thermal-annealing process are its in-situ, localized and two-dimensional treatment. The color of the $CO_2$ laser annealing region turns from light-yellow to dark-yellow by increasing $P_{laser}$ from 3 to 13.5 kW/cm$^2$ (see Fig. 27). The change in color of $SiO_x$ film is mainly attributed to the variation on the absorption coefficient and due to the precipitation of Si nanocrystals embedded in the $SiO_x$ film.

Since the as-grown $SiO_x$ film contains high concentration of hydrogen, the pre-annealing is used to obtain a hydrogen-free $SiO_x$ film owing to the release of hydrogen during annealing. To distinguish the shrinkage in $SiO_x$ film thickness either by $CO_2$ laser annealing induced de-hydrogenation or by $CO_2$ laser ablation process, the $SiO_x$ film was first de-hydrogenated by annealing either in a furnace at 1100$^o$C or with a $CO_2$ laser at $P_{laser}$ = 4 kW/cm$^2$ (well below ablation threshold). The thicknesses of annealed $SiO_x$ films are plotted as a function of the annealing time, as shown in Fig. 28. The de-hydrogenating process is finished after furnace annealing at 1100$^o$C for three hrs, while the thickness of the annealed $SiO_x$ film reduces from 281 to 242 nm. Similar result is also observed in the $CO_2$ laser annealed $SiO_x$ film after illuminating for 1.4 ms or longer. The shrinking depth of PECVD-grown $SiO_x$ film during annealing is about 38-39 nm. Since a

PECVD-grown $SiO_x$ film contains a high concentration of hydrogen, the compaction of $SiO_x$ film is attributed to the loss of hydrogen during annealing. To realize the optical damage threshold of $SiO_x$ films, the $CO_2$ laser ablation experiment was subsequently performed using the de-hydrogenated $SiO_x$ film with a thickness of 240 nm. This is done by annealing the $SiO_x$ film in atmosphere with a $CO_2$ laser at different intensities, and the ablation depth of the $SiO_x$ film measured as a function of $P_{laser}$ with a linear ablation slope of 29 nm/(kW/cm$^2$) at $P_{laser}$ > 6 kW/cm$^2$ is shown in Fig. 29.

Previously, an ArF pulsed excimer laser at 193 nm was first used to evaporate SiO powder with an energy deposition of 110 mJ/cm$^2$ per pulse, which is generally a laser sputtering process although a Si-$SiO_2$ phase separation was observed [47]. Rossi et al. [48] proposed the formation of Si nanocrystals with diameters ranging from 2.5 to 12 nm embedded in undoped amorphous $SiO_x$ film containing different oxygen content of 28, 35 and 40 % using continuous-wave (CW) $Ar^+$ laser ($\lambda$=514.5 nm) treatment at $P_{laser}$ = $10^5$ W/cm$^2$. In their experiment, the required $P_{laser}$ is much higher than that our condition using $CO_2$ laser, which is mainly due to the relatively small absorption coefficient of $1\times10^{-6}$ cm$^{-1}$ of $SiO_2$ material at 514.5 nm. The surface temperature is linear proportional to the absorption coefficient, however, absorption coefficients of the $SiO_2$ film at wavelengths from 200 to 3000 nm are much lower than that at 10.6 μm [44, 49]. Even though a pulsed Nd:YAG laser ($\tau$=8 ns, $\lambda$=355 nm) or KrF excimer laser ($\lambda$=248 nm) [50, 51] was employed to synthesize Si nanocrystals in $SiO_x$, a laser energy density of 30-85 mJ/cm$^2$ or $P_{laser}$ = 4-10 MW/cm$^2$ is still far beyond the laser ablation threshold. The absorption coefficient of the $SiO_2$ material at aforementioned wavelength range is too low to achieve enough temperature for synthesizing Si nanocrystals at $P_{laser}$ = 6 kW/cm$^2$ (near ablation threshold). To obtain similar annealing effect, a high-power laser illumination

process is mandatory. However, the structural damage is also associated with a high-power annealing process, which usually introduces other defects related effects in oxide materials.

The RBS spectrum of the as-grown $SiO_x$ film on the Si substrate shown in Fig. 30 reveals clear signals of Si and oxygen at 1.147 MeV and 742.0 keV, respectively. It also determines the thickness for the as-grown $SiO_x$ film as 280 nm, which is in good agreement with that measured using a surface profiler. The calculated O/Si ratio of 1.25 corresponds to a total Si concentration of 44.44 atomic %. That is, the as-grown $SiO_x$ film is $SiO_{1.25}$. The existence and the size distribution of Si nanocrystal embedded in $SiO_{1.25}$ film annealed at $P_{laser}$ = 6 kW/cm$^2$ is confirmed by cross-sectional HRTEM images (see Fig. 31). HRTEM images reveal that the average diameter of Si nanocrystals is about 5.3 nm. As shown in the inset of Fig. 5, the lattice space of one of Si nanocrystals embedded in $SiO_{1.25}$ is determined as 0.3 nm, which indicates the (111) plane of Si. Moreover, the diffractive pattern, with ring circles, of $SiO_{1.25}$ indicates that the orientation of Si nanocrystals is random, as shown in the inset of Fig. 31. The electron diffraction image showing clear ring patterns at different sections also evidences the existence of Si nanocrystals. In more detail, three cross-sectional HRTEM images revealing the similar size distribution of a thicker $SiO_{1.25}$ at different depths are shown in Fig. 31, which confirms the tiny change in annealing temperature distribution along the depth.

The surface density of Si nanocrystals buried in $SiO_{1.25}$ film annealed at $P_{laser}$ = 6 kW/cm$^2$ was estimated about $3.43\times10^{12}$ cm$^{-2}$, which was calculated from planar photographs of $SiO_x$ films taken by HRTEM. The thickness of $SiO_{1.25}$ was further reduced to 220 nm as determined by the cross-sectional HRTEM. The volume density ρ of Si nanocrystals buried in the $CO_2$ laser annealed $SiO_{1.25}$ film is $1.56\times10^{17}$ cm$^{-3}$ as estimated from planar and cross-sectional HRTEM images. Since Si exhibits

a diamond lattice structure with eight atoms in a unit cell. Taking the Si lattice constant of 0.543 nm, the number of Si atoms per cubic centimeter of $8/a^3 = 8/(5.43\times10^{-8})^3 = 5\times10^{22}$ atoms/cm$^3$ is obtained. The estimated average diameter and volume of Si nanocrystals are about 5.3 nm and $7.79\times10^{-20}$ cm$^3$, respectively. In this case, such a Si nanocrystal is constructed by nearly 3900 Si atoms. The atomic mass of $SiO_{1.25}$ becomes 48 amu, and the evaluated density of $SiO_{1.25}$ is 1.86 g/cm$^3$, which is determined by the net weight over the volume. Therefore, the number of Si atom per cubic centimeter of PECVD-grown $SiO_{1.25}$ film is calculated as $2.33\times10^{22}$ atoms/cm$^3$. As a result, the number of the excess Si atoms in the $SiO_{1.25}$ film is determined as $8.7\times10^{21}$ atoms/cm$^3$. With this value, the number of Si nanocrystals buried in $SiO_{1.25}$ film is about $2.23\times10^{18}$ cm$^{-3}$ as calculated using $N_{nc\text{-}Si} = (8.7\times10^{21}$ atoms/cm$^3)/(3900$ atoms/nc-Si). In comparison with the volume density of Si nanocrystals, $1.56\times10^{17}$ cm$^{-3}$, estimated from planar and cross-sectional HRTEM images, the theoretical result is higher than that determined by HRTEM by one order. Since the ablated depth of the laser annealed $SiO_{1.25}$ at 6 kW/cm$^2$ is about 20 nm, 10% of Si nanocrystals buried in $SiO_{1.25}$ film can be evaporated. Therefore, the concentration of $1.56\times10^{17}$ cm$^{-3}$ is much close to the concentration of $2.23\times10^{17}$ cm$^{-3}$, 10% of Si nanocrystals buried in $SiO_{1.25}$ film.

### 3.5.4 Photoluminescence and transmission spectra diagnosis of $CO_2$ laser-annealed PECVD grown Si-rich $SiO_2$

A broadband blue-green PL was observed in $SiO_{1.25}$ film after $CO_2$ laser annealing at $P_{laser} = 1.5$ kW/cm$^2$, as shown in Fig. 29(a). One of the decomposed peaks at 520

nm with 225nm linewidth is attributed to the E'$_\delta$ defect (a precursor of Si nanocrystal, denoted as [Si↑Si—Si]) [54], and the other at 455 nm with 115nm linewidth is contributed by neutral oxygen vacancy (NOV, denoted as [$O_3$≡Si-Si≡$O_3$]) center [55, 56]. As $P_{laser}$ increases, the blue-green PL corresponding to the E'$_\delta$ center and NOV defect were enhanced associated with narrowing linewidths of 176 nm and 99 nm, respectively. Afterwards, the intensity of the PL peak at 520 nm slightly increases in the $SiO_{1.25}$ sample laser-annealed at $P_{laser}$ of 3 kW/cm$^2$, which indicates a more pronounced activation of E'$_\delta$ defects than the NOV defects. This phenomenon is somewhat similar with that ever observed in a furnace-annealed $SiO_{1.25}$ film, as shown in Fig. 29. In comparison with previous studies [57, 58], the optimized furnace annealing time for the E'$_\delta$ defect is >4 hrs at 1100$^o$C, which is much longer than that of $CO_2$ laser annealing process. It is seen in Fig. 29(c) that the PL further red-shifts to the wavelength of 600-620 nm as $P_{laser}$ is increased to 4.5 kW/cm$^2$, indicating a diminish of NOV and other structural defects and the increasing density of small-size Si nanocrystals precipitated from E'$_\delta$ defects. A significant PL peak at 806 nm with 100nm linewidth is observed at $P_{laser}$ = 6.0 kW/cm$^2$, such an optimized $P_{laser}$ for precipitating Si nanocrystals in $SiO_{1.25}$ film is near the ablation threshold. Previously, a similar PL result attributed to the Si nanocrystal in the $SiO_x$ film with 39 atomic % of Si after annealing at 1250$^o$C for 1 hr was reported. [48]

In addition, a high-intensity $CO_2$ laser annealing process not only locally anneals the $SiO_{1.25}$ film and precipitates Si nanocrystals, but also introduces structural defects with PL at 400-600 nm nearby Si nanocrystals during such a short-term heat treatment. Most of these defects are oxygen dependent; some of them are NOV defects originated from the Si nanocrystal precipitation process as many excessive Si atoms occupied the sites of oxygen move away to precipitate Si nanocrystals. Precipitated

Si nanocrystals inevitably compress the $SiO_x$ matrix and result in the formation of the interstitial oxygen dependent new defects, such as the weak-oxygen bond or ionized oxygen molecule ($O_2^-$) [57, 58] at PL wavelength of 410 nm. Such a phenomenon was never observed in furnace annealed $SiO_x$ film since the high-temperature and long-term furnace annealing usually causes a gradual recovery on the compressing strain of $SiO_2$ matrix nearby Si nanocrystals. In addition, the slight red-shift of PL peak wavelength from 806 to 825 nm indicates an increase in size of Si nanocrystals as $P_{laser}$ increases further from 6 to 7.5 kW/cm$^2$. This result correlates well with previous observations that the PL red-shifts from 700 to 950 nm as furnace temperature increases from 1100 to 1250$^o$C [51]. However, the ablation of the $SiO_{1.25}$ film occurring at such high $P_{laser}$ also leads to another featured PL at 410 nm due to structural damage, as shown in Fig. 29(f). This results in a concurrent decrease in near-infrared PL intensity by one order of magnitude, whereas the intensity of the blue PL at 410 nm varies oppositely. In fact, the 410-nm PL intensity is increased by one order of magnitude as $P_{laser}$ increases from 7.5 to 11 kW/cm$^2$. After the $CO_2$ laser annealing process at $P_{laser}$ = 13.5 kW/cm$^2$, the whole $SiO_{1.25}$ layer is ablated.

The transmission spectra of the as-grown and $CO_2$ laser annealed $SiO_x$ film at near-infrared wavelength shows a similar transparent result with a transmission of >85 % as reported before [59, 60]. The absence of the near-infrared absorption in $CO_2$ laser annealed $SiO_x$ films indicates a small absorption cross-section or density of Si nanocrystals. Nonetheless, a slight red-shift on the transmission band edge of the as-grown $SiO_x$ film is observed as compared to that of the quartz substrate, corresponding to a shrinkage in optical bandgap of $SiO_{1.25}$ film from 5.21 to 2.43 eV, as shown in Fig. 32. This is attributed to the increasing oxygen non-bonding electronic states in $SiO_{1.25}$ near the valence band edge [61]. The valence band edge

moves up and the conduction edge simultaneously moves down as the Si-rich condition becomes significant, while the increased Si–Si bond states are gradually overlaid with the oxygen non-bonding states and finally spread out into the Si valence band. The net result is that the band gap decreases nonlinearly when Si concentration continually increases. The interference fringes occurred between 350 and 750 nm are attributed to the different refractive indexes of $SiO_{1.25}$ film and Quartz substrate caused by the 37 atomic % of Si atoms in $SiO_{1.25}$ film.

After annealing at $P_{laser}$ = 5.8 kW/cm$^2$ or higher, the $CO_2$ laser annealed $SiO_{1.25}$ film shows a stronger absorption between 400 and 600 nm than that of the as-grown $SiO_x$ or the quartz substrate. In comparison with the transmission spectra of the as-grown and $CO_2$ laser annealed $SiO_x$, a clear absorption spectrum between 350 and 600 nm was observed, and the optical bandgap of $CO_2$ laser annealed $SiO_{1.25}$ film in comparison with that of the as-grown $SiO_{1.25}$ film redshifts from 4.94 to 4.0 eV (see inset of Fig. 32). Several possibilities may be considered to red-shift the transmission spectrum band edge of the $CO_2$ laser annealed $SiO_{1.25}$ film, such as the generation of oxygen related defects and the varied composition of $SiO_{1.25}$ film. The red-shifted transmission spectrum is not attributed to Si nanocrystals, however, which coincides well with the defect related blue-green PL spectrum of $CO_2$ laser annealed $SiO_{1.25}$ film at $P_{laser}$ > 6 kW/cm$^2$. It is obvious that the red-shifted transmission spectrum was attributed to the absorption of NOV and weak-oxygen-bond defects due to the overlapping emission and absorption spectra. As $P_{laser}$ enlarges from 6 to 12 kW/cm$^2$, the transmission spectra of $SiO_x$ films illustrate blue-shifted phenomenon from 457 to 422 nm at a transmission of 50 %, as shown in Fig. 33. In particular, the transmission at 410 nm increases from 27 % at $P_{laser}$ = 6 kW/cm$^2$ to 43 % at $P_{laser}$ = 12 kW/cm$^2$under the decreasing thickness of $SiO_{1.25}$ film and the $CO_2$ laser ablation. Such an anomalous absorption directly confirms that the structure of $SiO_{1.25}$ film has

been severely damaged with numerous oxygen vacancy related defects during the $CO_2$ laser ablation.

Due to the significant change in the refractive index, a reflection spectrum of the $CO_2$ laser annealed $SiO_{1.25}$ film annealed at different $P_{laser}$ shows a strongly interfered fringe as compared to that of the quartz substrate or as-grown $SiO_{1.25}$ film, as shown in Fig. 34. The precipitation of Si nanocrystals embedded in $SiO_{1.25}$ film causes the increasing refractive index of $SiO_{1.25}$ film. The almost same reflection patterns of $CO_2$ laser annealed $SiO_{1.25}$ films at $P_{laser}$ > 5.8 kW/cm$^2$ reveal that the refractive index of $CO_2$ laser annealed $SiO_{1.25}$ films remain unchanged, as shown in Fig. 35. Since the excess Si density in $SiO_{1.25}$ film remains unchanged during the $CO_2$ laser annealing process, the precipitation density of Si nanocrystals will be saturated at a certain laser $P_{laser}$ and beyond. According to the fringe contrast of reflection spectra shown in Fig. 35, the refractive indexes of $CO_2$ laser annealed $SiO_{1.25}$ films as a function of $P_{laser}$ are calculated and shown in Fig. 36 using the ratio of the maximum to minimum reflectance, as given by $\frac{R(\max)}{R(\min)} = \frac{(R_1+R_2)(1-\sqrt{R_1R_2})^2}{(1+R_1R_2)(\sqrt{R_1}-\sqrt{R_2})^2}$ .[62] To confirm, a Bruggeman effective-medium approximation (BEMA) [63, 64] simulation is also used to estimate the refractive index of $CO_2$ laser annealed $SiO_{1.25}$ film at $P_{laser}$ = 6 kW/cm$^2$. Assuming that the composite material exhibits two phases with volume fractions $f$ and $1-f$, the effective complex dielectric function is calculated by $f_{nc-Si}\frac{\varepsilon_{nc-Si}-\varepsilon_{SiO_{1.25}}}{\varepsilon_{nc-Si}+2\varepsilon_{SiO_{1.25}}} + f_{SiO_2}\frac{\varepsilon_{SiO_2}-\varepsilon_{SiO_{1.25}}}{\varepsilon_{SiO_2}+2\varepsilon_{SiO_{1.25}}} = 0$, where $f_{nc-Si} + f_{SiO2} = 1$, $\varepsilon_{nc-Si}$, $\varepsilon_{SiO1.25}$, and $\varepsilon_{SiO2}$ are the dielectric functions of Si nanocrystal, the $CO_2$ laser annealed $SiO_{1.25}$ film, and the $SiO_2$ film, respectively. With a Si nanocrystal density of $1.56\times10^{17}$ cm$^{-3}$, the estimated refractive index of $CO_2$ laser annealed $SiO_{1.25}$ film at $P_{laser}$ = 6 kW/cm$^2$ is about 1.73 at 633 nm, which is close to the result in Fig. 36 obtained from reflection spectra. Similar refractive index of a thermally annealed $Si^+$ implanted $SiO_2$ was

also reported by Naciri et al. [65]. At the $P_{laser}$ below 3 kW/cm$^2$, the change in refractive index of $CO_2$ laser annealed $SiO_{1.25}$ film is less than 0.6 % since the precipitation of Si nanocrystals has not been initiated yet. The refractive index of $SiO_{1.25}$ film increases from 1.57 to 1.87 as the $P_{laser}$ increases from 1.5 to 7.5 kW/cm$^2$. That is, the Si nanocrystal precipitation becomes more pronounced at larger $P_{laser}$. The refractive indices of $SiO_x$ films with total Si concentrations of 39, 42, and 46 atomic % were previously determined as 1.84, 1.93 and 2.15, respectively [66]. Another study [67] also reports a slight increase in refractive index from 1.65 to 1.9 as the oxygen molar ratio of $SiO_x$ decreases from 1.85 to 1.45. These results strongly corroborate the increasing refractive index of a thermally annealed $SiO_x$ film with buried Si nanocrystals. The saturation on the refractive index of the $SiO_x$ film at higher $P_{laser}$ is attributed to the saturation on density and size of Si nanocrystals in $SiO_x$ with a constant excess Si concentration during annealing.

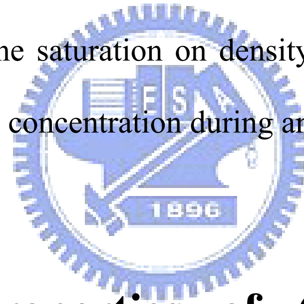


### 3.5.5 Electrical properties of $CO_2$ laser-annealed PECVD grown Si-rich $SiO_2$

During $CO_2$ laser annealing, the temperature $T(r, z)$ of the annealed $SiO_{1.25}$ film is expressed by the following equation: [68]

$$T(r,z) = \frac{4(1-R)}{\rho\, C_p} \times \frac{P_{laser}\, \tau}{\pi\, D^2\, d_{absorb}} \times \exp(\frac{-4r^2}{D^2}) \times \exp(-\alpha\, |z|)\,, \qquad (3\text{-}7)$$

where $r$, z, $\tau$, $\rho$ and $C_p$ are the radial distance, the depth, the illuminating time, the density and the specific heat of the $SiO_x$ film, respectively. [69] After $CO_2$ laser annealing at laser intensity ($P_{laser}$) of 6 kW/cm$^2$ and furnace annealing at 1100$^o$C for 30 min, broadband near-infrared PL spectra with peak wavelengths of 810 nm and

760 nm as well as spectral linewidths of 106 nm and 135 nm are observed (see Fig. 37(a) and 37(b)), respectively, which are attributed to the emission of nc-Si embedded in $SiO_{1.25}$. The estimated surface-temperature of the $SiO_{1.25}$ film at $P_{laser}$ of 6 kW/cm$^2$ was about 1350$^o$C. [70] The average size of nc-Si buried in $CO_2$ laser annealed $SiO_{1.25}$ is larger than that of furnace-annealed $SiO_{1.25}$, which contributes the decreasing bandgap of nc-Si and the redshift of PL peak wavelength from 760 to 810 nm. Another significant PL at 400-650 nm from the $CO_2$ laser-annealed sample is attributed to incomplete Si precipitation and slight damage of oxide matrix under $CO_2$ laser annealing within 1ms. Such a phenomenon has never been observed in the furnace-annealed sample since the high-temperature and long-term furnace annealing usually causes a gradual recovery on the compressing strain of the $SiO_2$ matrix nearby the nc-Si.

As the $CO_2$ laser intensity was larger than the ablation threshold of $SiO_x$ film (6 kW/cm$^2$), the surface of $SiO_x$ film was sputtered and damaged, which induced oxygen related irradiative defects. The ablation of the $SiO_x$ layer occurs at the $CO_2$ laser annealing of $P_{laser}$ = 12 kW/cm$^2$ and leads to another featured PL at 400 nm due to structural damage (see Fig. 37(c)). This results in a concurrent decrease in the near-infrared PL intensity by an order of magnitude, whereas the intensity of blue PL at 400 nm varies oppositely. In fact, the 400-nm PL intensity is increased by one order of magnitude as the $P_{laser}$ increases from 7.5 to 11 kW/cm$^2$, while the surface temperature has already exceeded the melting temperature of fused silica. Curve-fitting of the broadband PL spectrum from 350 nm to 700 nm reveals three peak wavelengths at 415 nm, 455 nm and 520 nm with associated linewidths of 40 nm, 66 nm and 113 nm as well as the associated irradiative defects of weak-oxygen-bond, neutral oxygen vacancy (NOV) defect and E'$_\delta$ center, respectively. Most of these defects are oxygen dependent; and some of them are NOV defects originated from the

nc-Si precipitation process as many excessive Si atoms occupied the sites of oxygen move away to precipitate nc-Si. Precipitated nc-Si inevitably compresses the $SiO_x$ matrix and results in the formation of the interstitial oxygen dependent new defects, such as the weak-oxygen bond or ionized oxygen molecule ($O_2^-$).

The turn-on voltages of ITO/$CO_2$ laser RTA $SiO_x$/p-Si/Al and ITO/furnace-annealed $SiO_x$/p-Si/Al MOSLEDs are 79 and 87 V with slopes of 2.7 and 2.2 (kV/A/$cm^2$), respectively. Lower turn-on voltage and higher slope of an ITO/$CO_2$ laser RTA $SiO_x$/p-Si/Al MOSLED are attributed to the existence of defects buried in $CO_2$ laser RTA $SiO_x$ film. The electric-field ($E$) dependent emission current ($I$) can be described and the current-field plot can thus be fitted by Fowler-Nordheim (FN) tunneling equations (3-4): [32]

The FN tunneling behavior can be confirmed, due to the linear transferred function characteristic in the Arrhenius FN plot (see Fig. 38). The threshold electric-fields to initiate FN tunneling for $CO_2$ RTA and furnace-annealed MOSLEDs are 1.8 and 3.2 MV/cm, respectively, which indicates that the effective potential barrier of the sample becomes smaller with the assistance of defects. This essentially corroborates with the reduction on threshold electric-field of FN tunneling occurred in the $CO_2$ laser RTA sample. The gradient of power-current (P-I) plot of ITO/$CO_2$ laser RTA $SiO_x$/p-Si/Al and ITO/furnace-annealed $SiO_x$/p-Si/Al MOSLEDs are 33.5 and 17.6 (μW/A/$cm^2$), respectively (see Fig. 39). The EL power of the ITO/$CO_2$ laser RTA $SiO_x$/p-Si/Al MOSLED with oxygen-related defects can be enlarged by two times as compared to that of the ITO/furnace-annealed $SiO_x$/p-Si/Al MOSLED with a higher turn-on voltage.

The barrier height of ITO-$SiO_x$ junction is 3.7 eV with electric affinities of 4.7 eV for ITO and 1 eV for $SiO_2$. The electric affinity and bandgap of Si substrate are 4 eV and 1.12 eV, respectively. Due to the $CO_2$ rapid-laser-annealing process

introduces oxygen-related defects buried in the ITO/$CO_2$ laser RTA $SiO_x$/p-Si/Al MOSLED, these oxygen correlated defects and interfacial states facilitate the carrier transport into nc-Si for the electron-hole pair recombination (see the inset of Fig. 39), and also decrease the turn-on voltage. This also elucidates the significant reduction of threshold electric-field of the ITO/$CO_2$-laser-RTA $SiO_x$/p-Si/Al MOSLED. In contrast to the conventional furnace-annealed MOSLED, the high-temperature and long-term furnace-annealing usually causes a gradual recovery on the compressing strain of the $SiO_2$ matrix nearby the nc-Si and also contributes a defect-free furnace-annealed $SiO_x$ film, corresponding to the higher turn-on voltage, lower EL power and the difficulty of carrier injection into nc-Si. Consequently, the electrons require a higher electric-filed to tunnel through the barriers of the MOS structure. Furthermore, the enhanced P-I slope and EL power from the $CO_2$ laser RTA $SiO_x$ based MOSLED are due to the assistance of carrier injection via oxygen-related defects as compared to those of the furnace-annealed $SiO_x$ based MOSLED at same biased condition.

Nc-Si related EL spectra of ITO/$CO_2$ laser RTA $SiO_x$/p-Si/Al MOSLED with a bright color pattern was decomposed into three luminescent peaks at 590, 715 and 810 nm with the spectral linewidths of 203, 117 and 54 nm as well as peak ratios of 1.65:1.47:1, respectively (see the lower of Fig. 40). The luminescent peaks at 590 and 810 nm emitting from different size of nc-Si were observed, however, the luminescent peak at 715 nm was not obviously found in the PL spectrum. Because of oxygen-related defects, such as weak-oxygen-bond and NOV defects, behave high energy bandgaps, carriers favor to inject into smaller nc-Si with higher energy bandgaps and approximate excited level via oxygen-related defects, and then recombine in the nc-Si. This result corresponds to the largest decomposed-EL intensity at 590 nm and the reduction of the decomposed-EL intensity as the

increasing size of nc-Si. Hence, the EL emission from nc-Si at 715 nm can be enhanced and observed. The EL spectrum of ITO/furnace-annealed $SiO_x$/p-Si/Al MOSLED, biased at higher electric-field without the carrier-transport assistant of oxygen-related defects, reveals a deep-red EL pattern (see the upper inset in Fig. 40) and dual luminescent peaks at wavelengths of 625 and 768 nm with spectral linewidths of 189 and 154 nm, respectively. The EL component at longer wavelength coincides well with that of PL, revealing that the nc-Si-related PL and EL are attributed to the same carrier recombination mechanism. The mechanism of secondary EL peak expanded to shorter-wavelength region (500-700 nm) is possibly attributed to the cold-carrier-tunneling process under appropriate bias. [54] Since the band bending becomes serious under an extremely high electric-field, leading to the carriers between adjacent nc-Si tunneled from first-order quantized state (n=1) to second-order quantized state (n=2), providing a higher population in the second-order state as well as an enhanced spontaneous emission at larger energy.

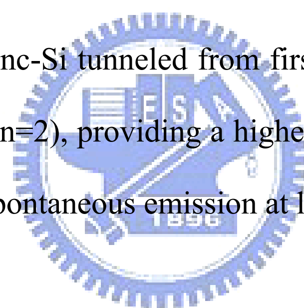

## 3.6 Conclusion

The structural and optical aspects of the localized synthesized Si nanocrystals in $SiO_{1.25}$ film using a $CO_2$ laser rapid thermal annealing process at nearly ablation threshold $P_{laser}$ = 5.8 kW/cm$^2$ is characterized. Due to the relatively high absorption coefficient of $SiO_2$ material at 10.6 μm, the required $P_{laser}$ is much lower than those at other wavelengths. The thickness of $SiO_{1.25}$ film was thinned from 280 to 240 nm during the dehydrogenating process at $P_{laser}$ = 4 kW/cm$^2$ for 1.4 ms. The color of $SiO_{1.25}$ film changes from light yellow to dark yellow is due to both the increasing absorption coefficient and refractive index of $SiO_{1.25}$ film. HRTEM analysis reveals the average diameter and density of 5.3 nm and $1.56\times10^{17}$ cm$^{-3}$, respectively, for the

precipitated Si nanocrystals in the annealed $SiO_x$ film. The Si nanocrystal dependent PL were observed at 806 nm or longer, whereas the $CO_2$ laser ablation at $P_{laser} > 6$ kW/cm$^2$ damages the $SiO_{1.25}$ film and induces significant blue PL at 410 nm by oxygen-related structural defects. Such a phenomenon was never observed in furnace annealed $SiO_x$ film since the high-temperature and long-term furnace annealing usually causes a gradual recovery on the compressing strain of $SiO_2$ matrix nearby Si nanocrystals. The refractive index of $SiO_{1.25}$ changes from 1.57 to 1.87 with increasing $P_{laser}$ as calculated from the reflection spectra with an enlarged interference fringe amplitude. In comparison with that of the quartz substrate or an as-grown sample, the red-shifted optical bandgap energy of a $CO_2$ laser annealed $SiO_{1.25}$ film from 5.21 to 2.43 eV has evidenced the effect of oxygen vacancy defects on the strong blue-green absorption. The enhanced near-infrared EL of an ITO/$CO_2$ laser RTA $SiO_x$/p-Si/Al MOSLED is preliminarily demonstrated. Dense nc-Si can be synthesized in the $SiO_{1.25}$ film by using $CO_2$ laser RTA at $P_{laser}$ of 6 kW/cm$^2$ for 1 ms. The comparison on PL spectra of $CO_2$ laser annealed and furnace-annealed PECVD-grown $SiO_{1.25}$ samples reveals the contribution of oxygen related defects. Since the $CO_2$ laser annealing time is only 1 ms and much shorter than furnace-annealing time (3 hours), the annealing time is insufficient for precipitating larger-size nc-Si, whereas the oxygen-related defects are generated in the $CO_2$ laser annealed $SiO_x$ film. These defects enhance the carrier transport through the MOSLED, reducing the tunneling threshold from 3.2 to 1.8 MV/cm as compared to the furnace-annealed sample. The elucidation on the role of the oxygen-related defects played on the improved carrier transport and enhanced light emission properties is addressed. A maximum EL power of nearly 50 nW from the ITO/$CO_2$ laser RTA $SiO_x$/p-Si/Al MOSLED under a biased voltage of 85 V and current density of 2.3 mA/cm$^2$ is reported to date.

# References

[1] G.-R. Lin, C. J. Lin, C. K. Lin, L. J. Chou, and Y. L. Chuen, J. Appl. Phys. **97**, 094306 (2005).

[2] M. Watanabe, T. Matsunuma, T. Maruyama, and Y. Maeda, Jpn. J. Appl. Phys. **37**, L591 (1998).

[3] C. H. Cho, B. H. Kim, and S. J. Park, Appl. Phys. Lett. **89**, 013116 (2006).

[4] G. Pucker, P. Bellutti, C. Spinella, K. Gatterer, M. Cazzanelli, and L. Pavesi, J. Appl. Phys. **88**, 6044, (2000).

[5] M. B. Park and N. H. Cho, Appl. Surf. Sci. **190**, 151 (2002).

[6] G.-R. Lin, C.-J. Lin and K.-C. Yu, J. Appl. Phys. **96,** 3025 (2004).

[7] T. Shimizu-Iwayama, N. Kurumado, D. E. Hole and D. E. Townsend, J. Appl. Phys. **83**, 6018 (1998).

[8] M. L. Brongersma, A. Polman, K. S. Min, E. Boer, T. Tambo and H. A. Atwater, Appl. Phys. Lett. **72**, 2577 (1998).

[9] L. Skuja, J. Non-Cryst. Solids **149**, 77 (1992).

[10] L. B. Ma, A. L. Ji, C. Liu, Y. Q. Wang and Z. X. Cao, J. Vac. Sci. Techol. B **22,** 2654 (2004).

[11] Y. Q. Wang, G. L. Kong, W. D. Chen, H. W. Diao, C. Y. Chen, S. B. Zhang and X. B. Liao, Appl. Phys. Lett. **81**, 4174 (2002).

[12] G.-R. Lin and C.-J. Lin, J. Appl. Phys. **95**, 8482 (2004).

[13] C.-J. Lin and G.-R. Lin, IEEE J. Quantum Electron. **41**, 441 (2005).

[14] G.-R. Lin, C.-J. Lin, C.-K. Lin, L.-J. Chou and Y.-L. Chueh, J. Appl. Phys. **97**, 4306 (2005).

[15] C. Garcia, B. Garrido, P. Pellegrino, R. Ferre, J. A. Moreno, J. R. Morante, L. Pavesi and M. Cazzanelli, Appl. Phys. Lett. **82**, 1595 (2003).

[16] C. J. Lin, C. K. Lin, C. W. Chang, Y. L. Chueh, H. C. Kuo, Eric W. G. Diau, L. J. Chou, and G.-R. Lin, Jpn. J. Appl. Phys., **45**, 1040 (2006).

[17] H. Morisaki, F. W. Ping, H. Ono, and K.Yazawa, J. Appl. Phys. **70**, 1869 (1991).

[18] O. Madelung, *Introduction to Solid State Theory*, Chap. 6, Springer-Verlag, Berlin (1996).

[19] S. Donati, *Photodetectors Devices, Circuits, and Applications*, p. 11, Prentice Hall, Englewood Cliffs, NJ (2000).

[20] F. Priolo, G. Franzo, D. Pacifici, V. Vinciguerra, F. Iacona, and A. Irrera, J. Appl. Phys. **89**, 264 (2001).

[21] D. Kovalev, J. Diener, H. Heckler, G. Polisski, N. Kunzner, and F. Koch, Phys. Rev. B **61**, 4485 (2000).

[22] C. Garcia, B. Garrido, P. Pellegrino, R. Ferre, J. A. Moreno, J. R. Morante, L. Pavesi, and M. Cazzanelli, Appl. Phys. Lett. **82**, 1595 (2003).

[13] B. H. Augustine, E. A. Irene, Y. J. He, K. J. Price, L. E. McNeil, K. N. Christensen, and D. M. Maher, J. Appl. Phys. **78**, 4020 (2000).

[14] C. Delerue, G. Allan, and M. Lannoo, Phys. Rev. B **48**, 11024 (1993).

[25] S. H. Bauer and John A. Haberman, IEEE J. Quantum Electron., **QE-14**, 233 (1978).

[26] T. A. Cleland and D. W. Hess, *J. Electrochem. Soc.*, **136**, 3103 (1989).

[27] T. K. S. Wong, B. Liu, B. Narayanan, V. Ligatchev, and R. Kumar, *Thin Solid Films*, **462-463**, 156 (2004).

[28] M. Lenzlinger and E. H. Snow, *J. Appl. Phys.*, **40**, 278 (1969).

[29] T. Z. Lu, M. Alexe, R. Scholz, V. Talelaev, and M. Zacharias, Appl. Phys. Lett., **87**, 202110 (2005).

[30] D. K. Schroder, “*Semiconductor Material and Device Characterization*” 2nd ed., p. 408 (John Wiley & Sons, Inc., New York, 1998).

[31] K. F. Schuegraf and C. M. Hu, Semicond. Sci. Technol. **9**, 989 (1994).

[32] R. H. Fowler and L. W. Nordheim, Proc. R. Soc. London, Ser. A, **119**, 173 (1928).

[33] E. H. Rhoderick and R. H. Williams, "Metal-Semiconductor Contacts" 2nd ed., Clarendon, Oxford, 1988.

[34] J. Frenkel, Phys. Rev. **54**, 657 (1938).

[35] J. R. Yeargan and H. L. Taylor, J. Appl. Phys. **39**, 5600 (1968).

[36] R. C. Hughes, Phys. Rev. Lett. **30**, 1333 (1973).

[37] L. Pavesi, L. Dal Negro, C. Mazzoleni, G. Franzo, and F. Priolo, Nature **408**, 440 (2000).

[38] G.-R. Lin, K. C. Yu, C. J. Lin, H. C. Kuo and M. C. Ou-Yang, Appl. Phys. Lett. **85**, 1000 (2004).

[39] H. C. Pan, C. C. Chou and H. L. Tsai, Appl. Phys. Lett. **83**, 3156 (2003).

[40] Q. He, M. H. Hong, W. M. Huang, T. C. Chong, Y. Q. Fu and H. J. Du, J. Micromech. and Microeng. **14**, 950 (2004).

[41] H. Gleskova, V. V. Ilchenko, V. A. Skryshevsky and V. I. Strikha, J. Phys. **43**, 169 (1993).

[42] V. S. Serbesov, P. A. Atanasov and R. I. Tomov, J. Mater. Sci. **5**, 272 (1994).

[43] N. F. Wang, M. P. Houng and Y. H. Wang, Jpn. J. Appl. Phys. Pt. 1 **38**, 5227 (1999).

[44] E. D. Palik, Handbook of Optical Constants of Solids, Academic Press, Washington, 762 (1985).

[45] G.-R. Lin, C. J. Lin, C. K. Lin, L. J. Chou and Y. L. Chueh, J. Appl. Phys. **97**, 094306 (2005).

[46] G.-R. Lin and C. J. Lin, J. Appl. Phys. **95**, 8484 (2004).

[47] F. Rochet, G. Dufour, H. Roulet, B. Pelloie, J. Perriere, E. Fogarassy, A. Slaoui, M. Froment, Phys. Rev. B **37**, 6468 (1999).

[48] M. C. Rossi, S. Salvatori, F. Galluzzi and G. Conte, Mater. Sci. Eng. B **69-70**, 299 (2000).

[49] F. Iacona, G. Franzo, E. C. Moreira, D. Pacifici, A. Irrera and F. Priolo, Mater. Sci. Eng. C **19**, 377 (2002).

[50] A. Janotta, Y. Dikce, M. Schmidt, C. Eisele, M. Stutzmann, M. Luysberg and L. Houben, J. Appl. Phys. **95**, 4060 (2004).

[51] B. Gallas, C.-C. Kao, S. Fisson, G. Vuye, J. Rivory, Y. Bernard and C. Belouet, Appl. Surf. Sci. **185**, 317 (2002).

[52] J. F. Ziegler, The Stopping and Range of Ions in Solids, Pergamon Press, New York, 1985.

[53] D. R. Linde, Handbook of Chemistry and Physics, CRC Press, Boca Raton, FL, 1991.

[54] G.-R. Lin and C. J. Lin, J. Appl. Phys. **95**, 8484 (2004).

[55] G.-R. Lin, C. J. Lin and. K. C. Yu, J. Appl. Phys. **96**, 3025 (2004).

[56] H. Nishikawa, R. Nakamura and J. H. Stathis, Phys. Rev. B **60**, 15910 (1999).

[57] C. J. Lin and G.-R. Lin, IEEE J. Quantum Electron. **41**, 441 (2005).

[58] J. C. Cheang-Wong, A. Oliver, J. Roiz, J. M. Hernánaez, L. Rodríguez-Fernández, J. G. Morales and A. Crespo-Sosa, Nucl. Instrum. Methods Phys. Res. B **175**, 490 (2001).

[59] L. Khriachtchev, M. Räsänen and S. Novikov, Appl. Phys. Lett. **83**, 3018 (2003).

[60] R. G. Elliman, M. J. Lederer and B. Luther-Davies, Appl. Phys. Lett. **80**, 1325 (2002).

[61] X. Y. Chen, Y. F. Lu, L. J. Tang, Y. H. Wu, B. J. Cho, X. J. Xu, J. R. Dong and W. D. Song, J. Appl. Phys. **97**, 014913 (2005).

[62] J. Hawkes and I. Latimer, Lasers: *Theory and Practice*, Prentice-Hall, 227 (1995).

[63] D. A. G. Bruggeman, Ann. Phys. **24**, 636 (1935).

[64] B. Abeles and J. I. Gittleman, Appl. Opt. **15**, 10 (1976).

[65] A. En Naciri, M. Mansour, L. Johann, J. J. Grob and C. Eckert, Nucl. Instr. and Meth. B **216**, 167 (2004).

[66] G. Vijaya Prakash, M. Cazzanelli, Z. Gaburro, L. Pavesi, F. Iacona, G. Franzo and F. Priolo, J. Mod. Opt. **49**, 719 (2002)

[67] L. Khriachtchev, M. Rasanen, S. Novikov, and L. Pavesi, Appl. Phys. Lett. **85**,

1511 (2004).

[68] T. R. Shiu, C. P. Grigoropoulos, D. G. Cahill, and R. Greif, J. Appl. Phys. **86**, 1311 (1999).

[69] C. J. Lin, G.-R. Lin, Y. L. Chueh, and L. J. Chou, Electrochem. Solid-State Lett. **8**, D43 (2005).

[70] G.-R. Lin, C. J. Lin, L. J. Chou, and Y. L. Chueh, J. Nanosci. Nanotechnol. **6**, 3710 (2006).

# Table

Table 1. $N_2O$ flucences, $SiH_4$ flucences and substrate temperatures of different samples.

| | A2 | A7 | A8 | A9 | A12 | A13 | A14 | A17 |
|---|---|---|---|---|---|---|---|---|
| $N_2O$ (sccm) | 90 | 120 | 150 | 180 | 120 | 120 | 120 | 120 |
| $SiH_4$ (sccm) | 30 | 30 | 30 | 30 | 30 | 30 | 30 | 30 |
| Temp. ($^oC$) | 100 | 100 | 100 | 100 | 200 | 250 | 300 | 350 |

Table 2. The wavelength, size, lifetime and estimated density of nc-Si in $SiO_x$ films after annealing for 15, 30 and 60 min.

| | | 15 min | 30 min | 60 min |
|---|---|---|---|---|
| Wavelength | (nm) | 761 | 751 | 743 |
| nc-Si Size | (nm) | 4.2 | 4.1 | 4.0 |
| Lifetime | (μs) | 52 | 31 | 20 |
| Estimated Density | ($cm^{-3}$) | $8.3\times10^{18}$ | $2.4\times10^{18}$ | $1.2\times10^{18}$ |

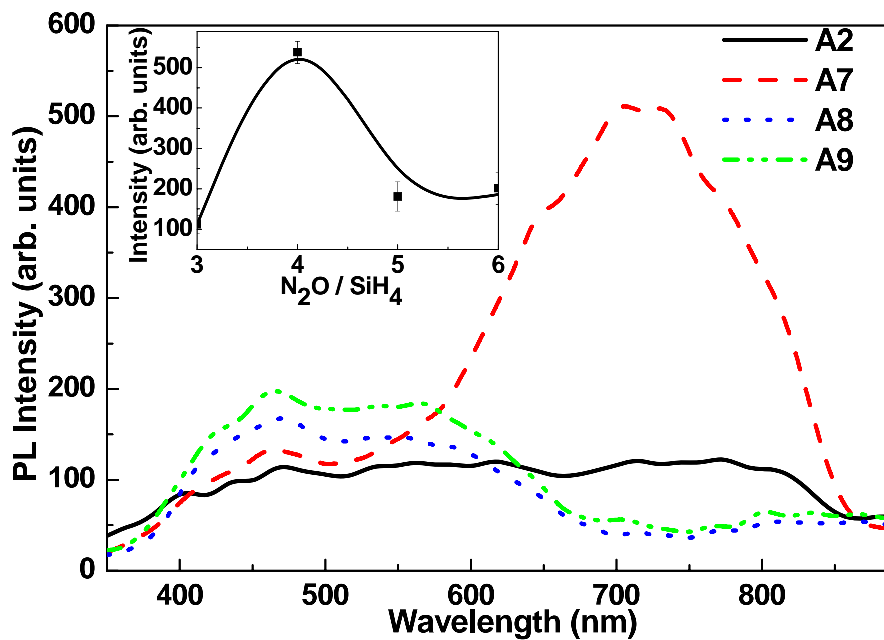


Fig. 1 PL spectra of 3-h-annealed Si-rich $SiO_x$ films fabricated by PECVD with different $N_2O/SiH_4$ ratios. The inset shows the peak intensity as a function of the $N_2O/SiH_4$ ratio.

1896

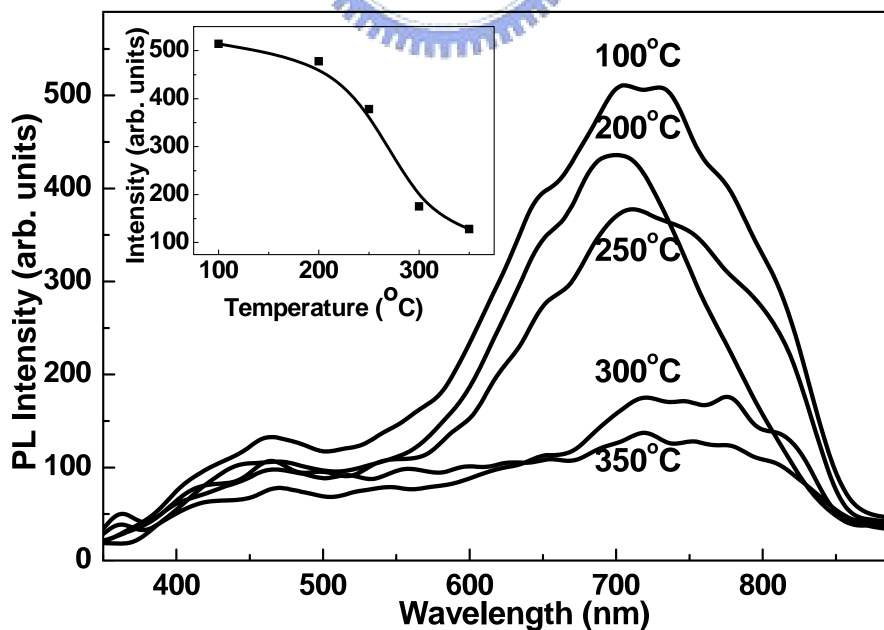


Fig. 2 Room-temperature PL spectra of annealed Si-rich $SiO_x$ films fabricated by PECVD with different substrate temperatures from 100 to 350°C. The inset shows the peak intensity as a function of substrate temperature.

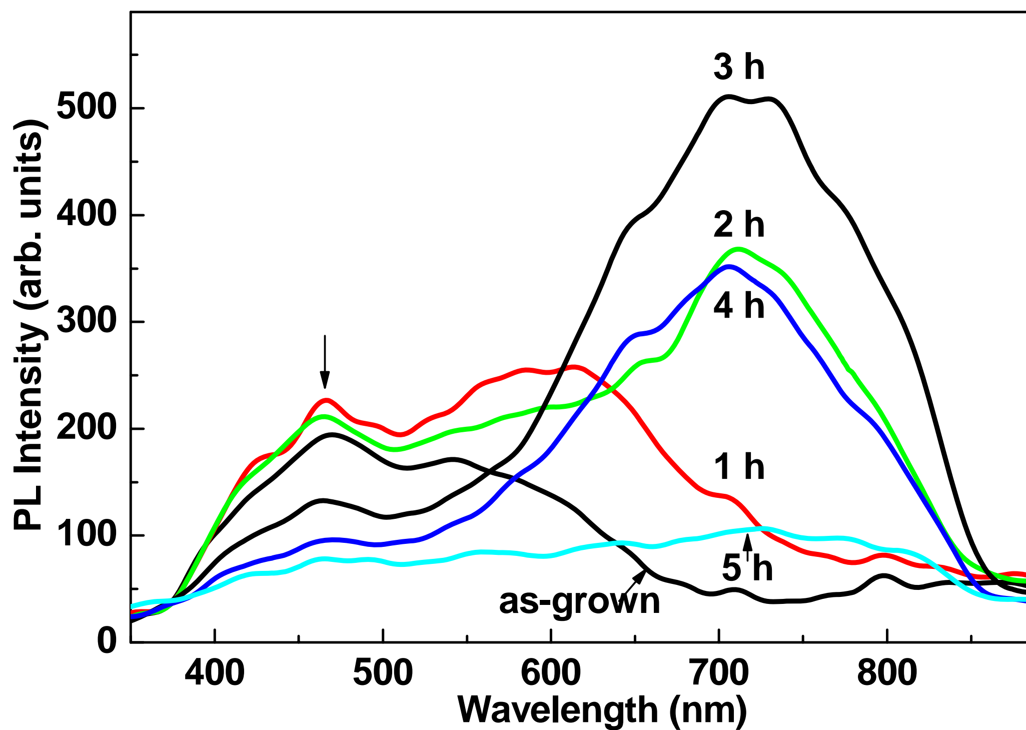


Fig. 3 PL spectra of as-grown sample A7 after annealing at 1100 °C for 1-5 h.

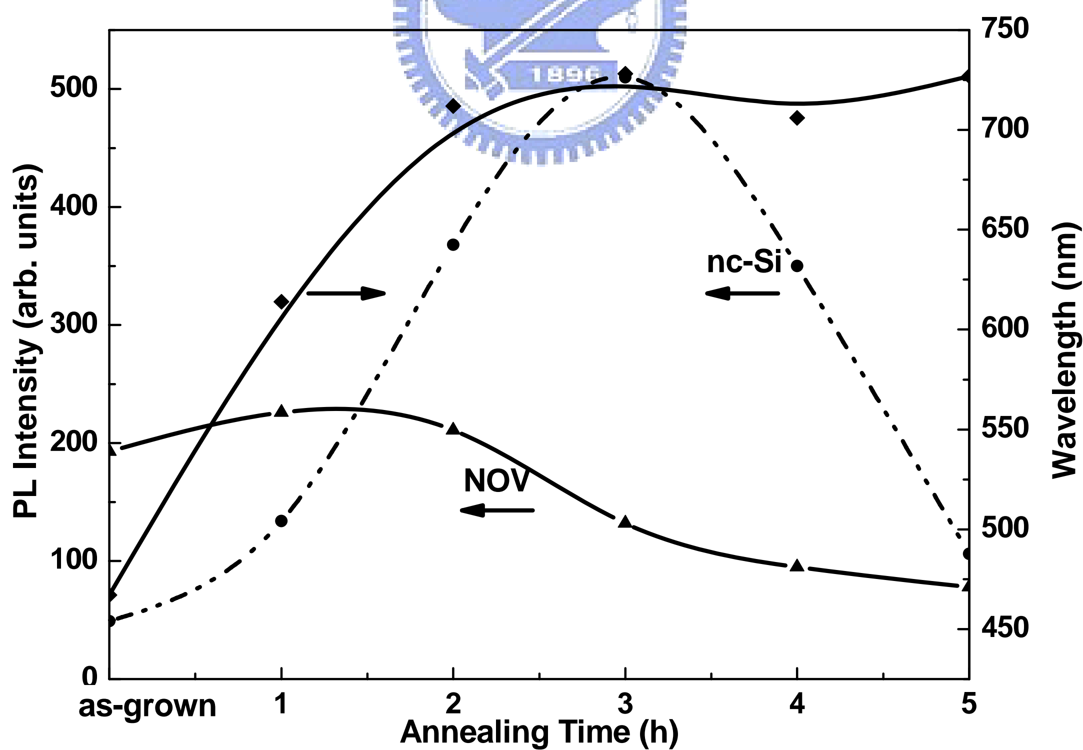


Fig. 4 Peak PL intensities of NOV defect and nc-Si, and peak wavelength of nc-Si as a function of the annealing time.

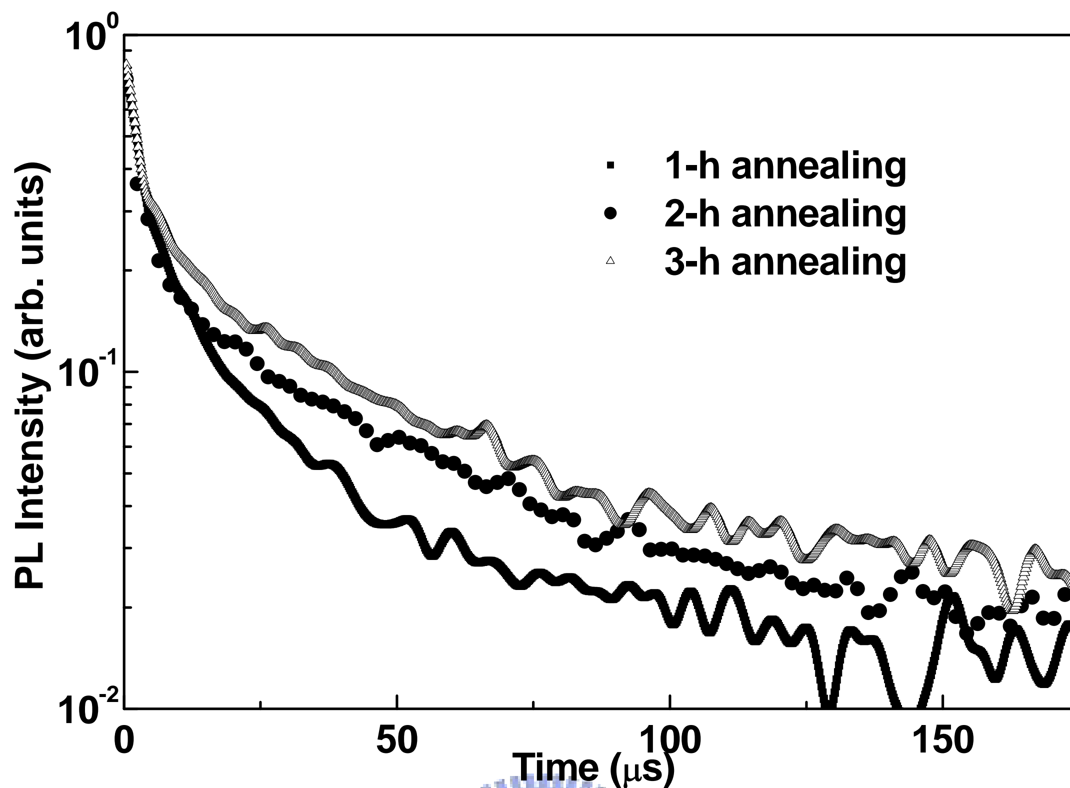


Fig. 5 Time-resolved PL traces of sample A7 after annealing at 1100 °C for 1, 2, and 3 h.

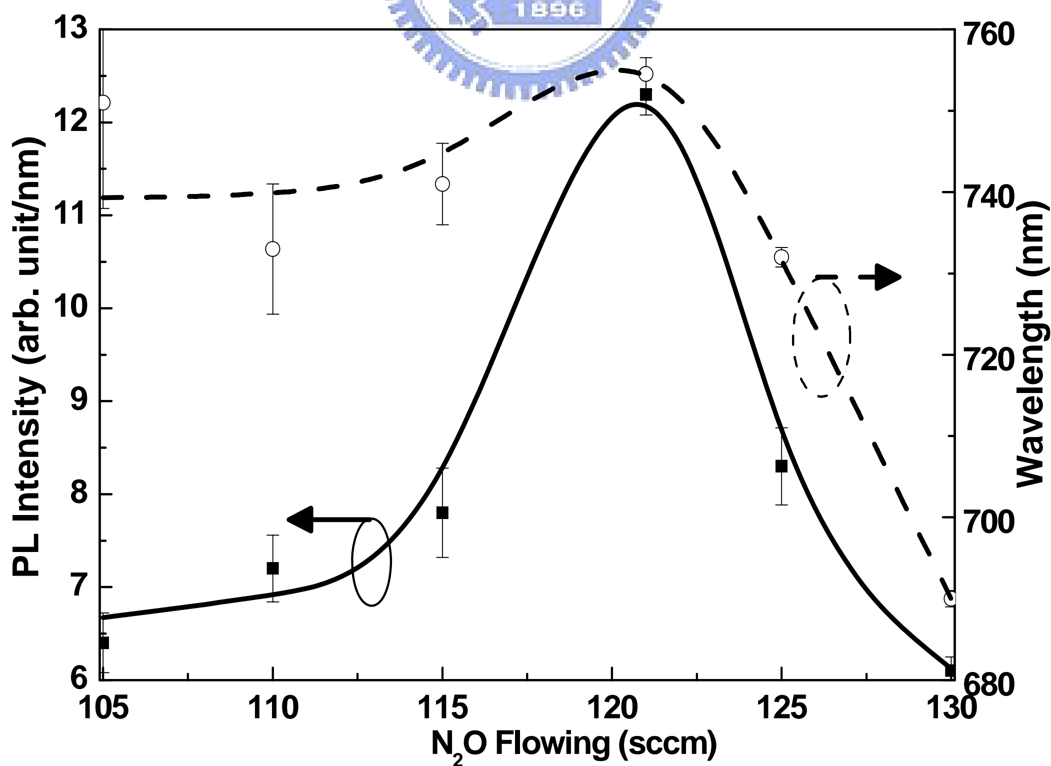


Fig. 6 PL intensity and peak wavelength as a function of $N_2O$ fluence.

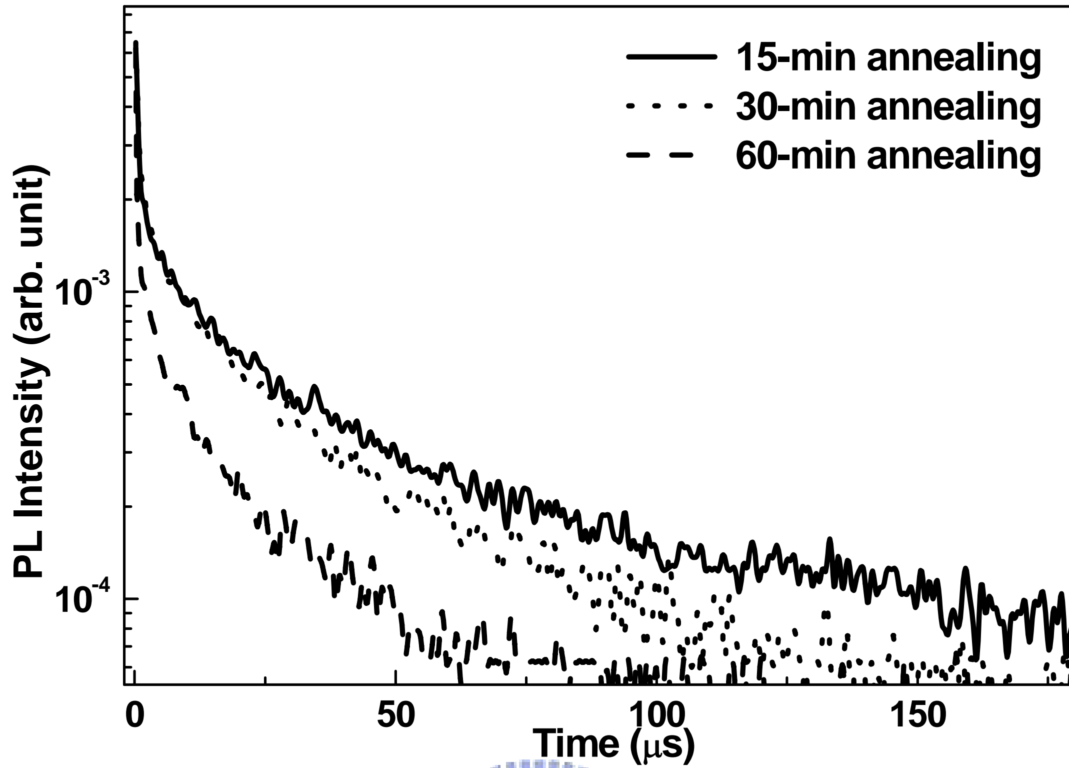


Fig. 7 TRPL spectra of nc-Si embedded in PECVD-grown $SiO_x$ samples for different annealing time.

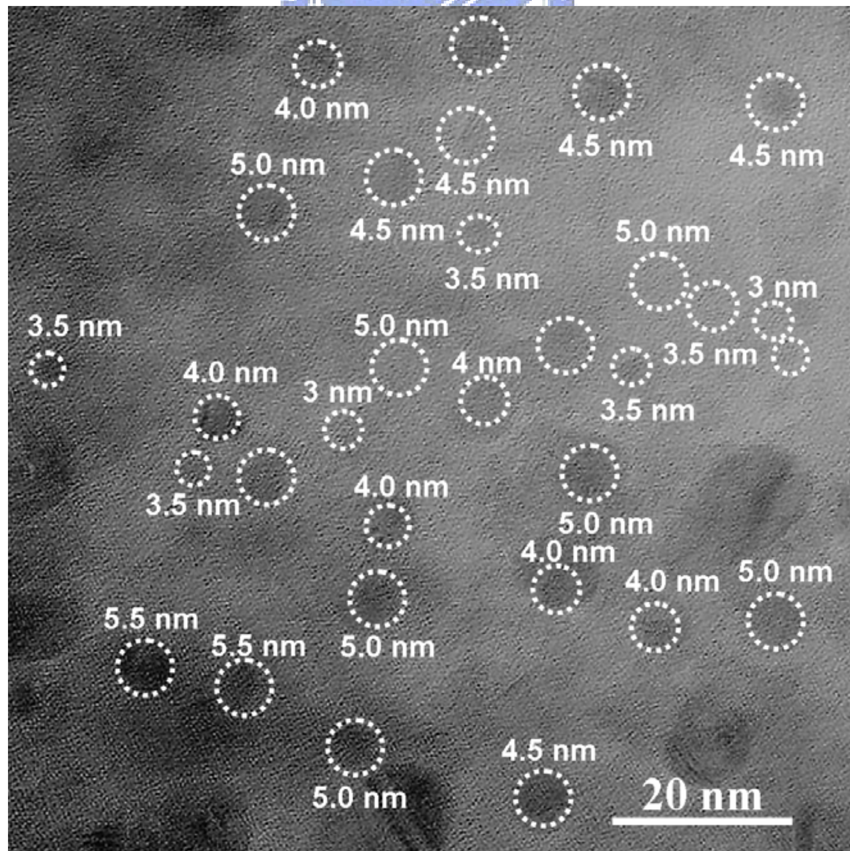


Fig. 8 Planar-view HRTEM picture of 15 min-annealed PECVD-grown $SiO_x$ film.

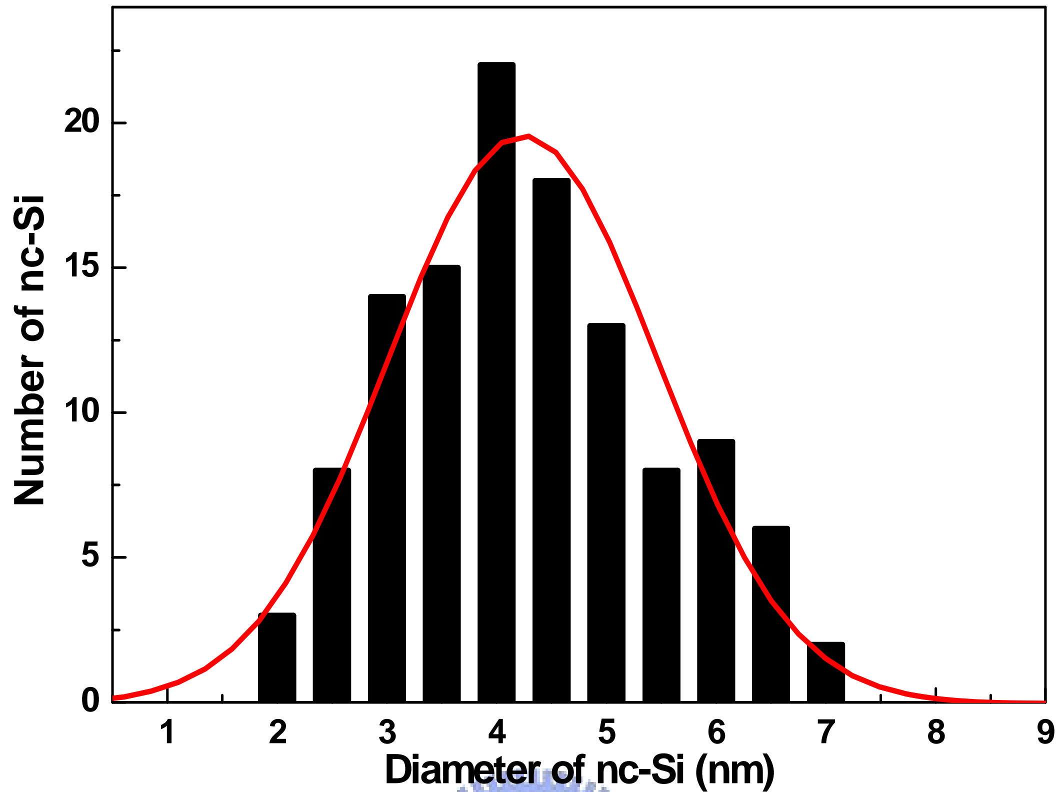


Fig. 9 Size distribution of nc-Si in the 15 min-annealed PECVD-grown $SiO_x$ film.

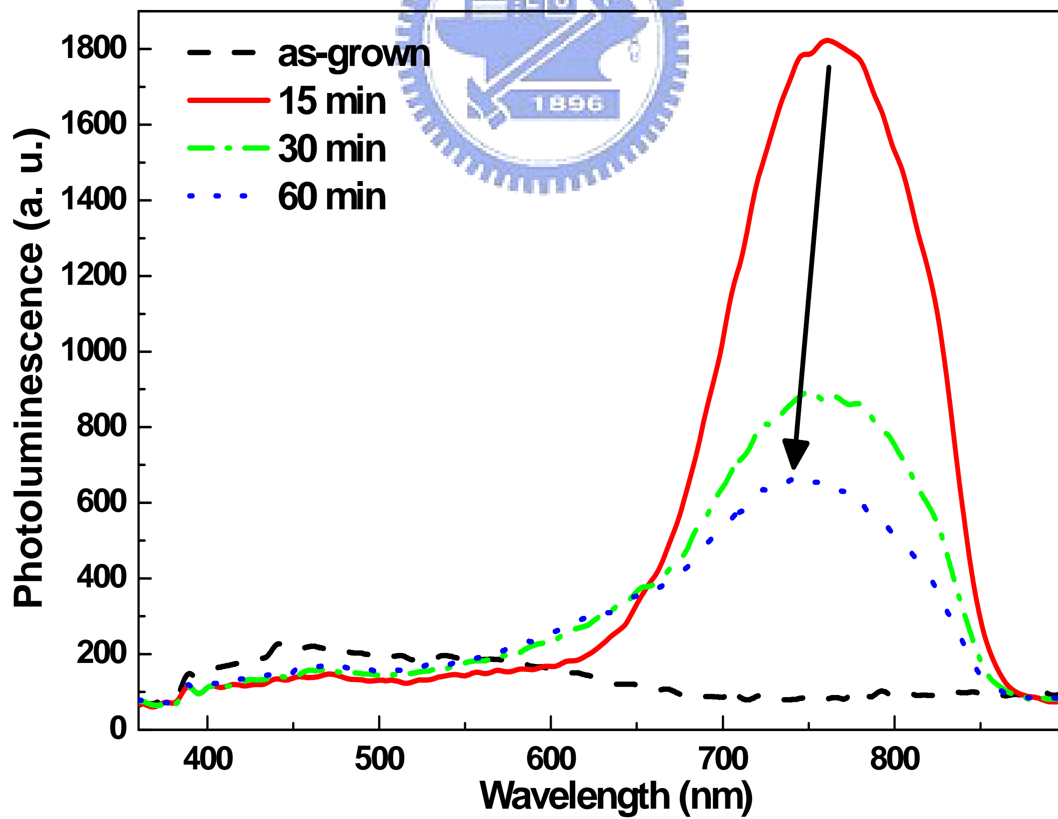


Fig. 10 PL spectra of PECVD-grown $SiO_x$ samples annealed from 15 to 60 min.

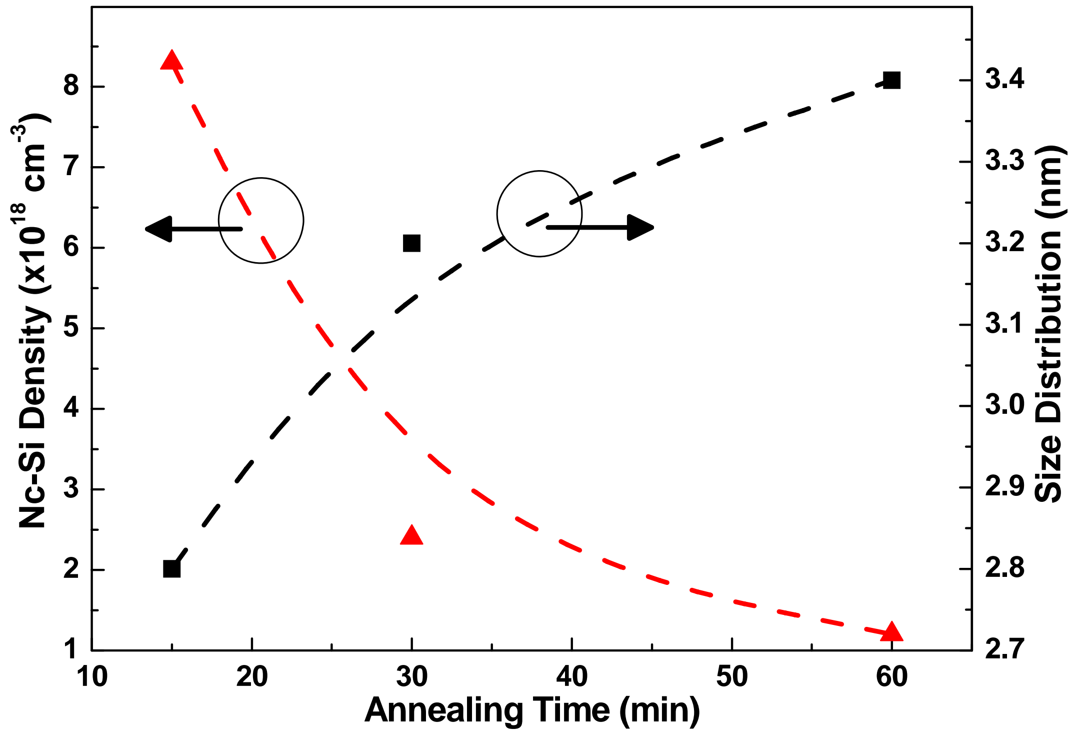


Fig. 11 Density and size distribution of nc-Si buried in annealed $SiO_x$ film as a function of annealing time.

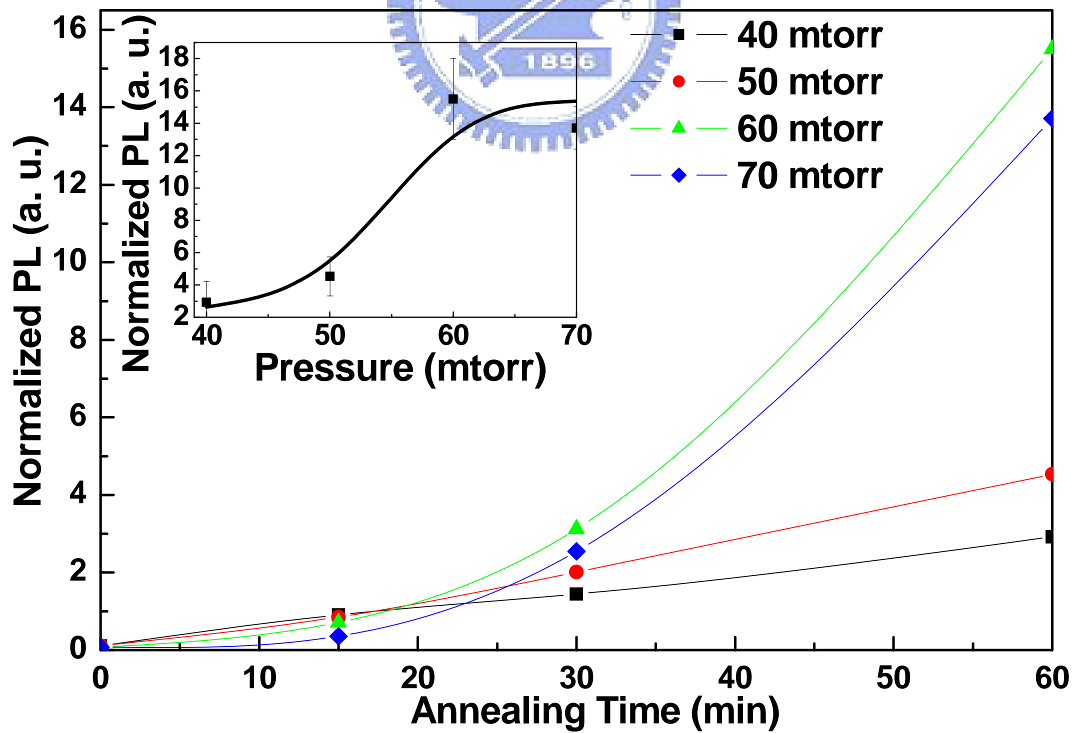


Fig. 12 PL as function of annealing time at different process pressures.

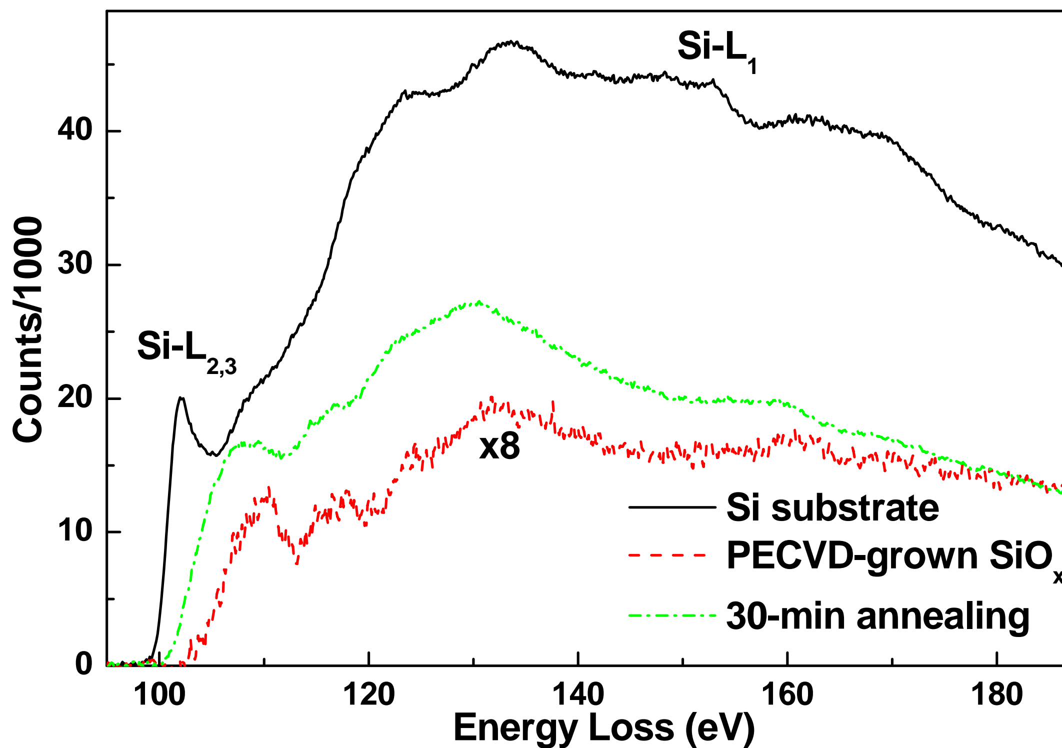


Fig. 13 EELS spectra of pure Si, as-grown $SiO_x$ and 30 min-annealed samples.

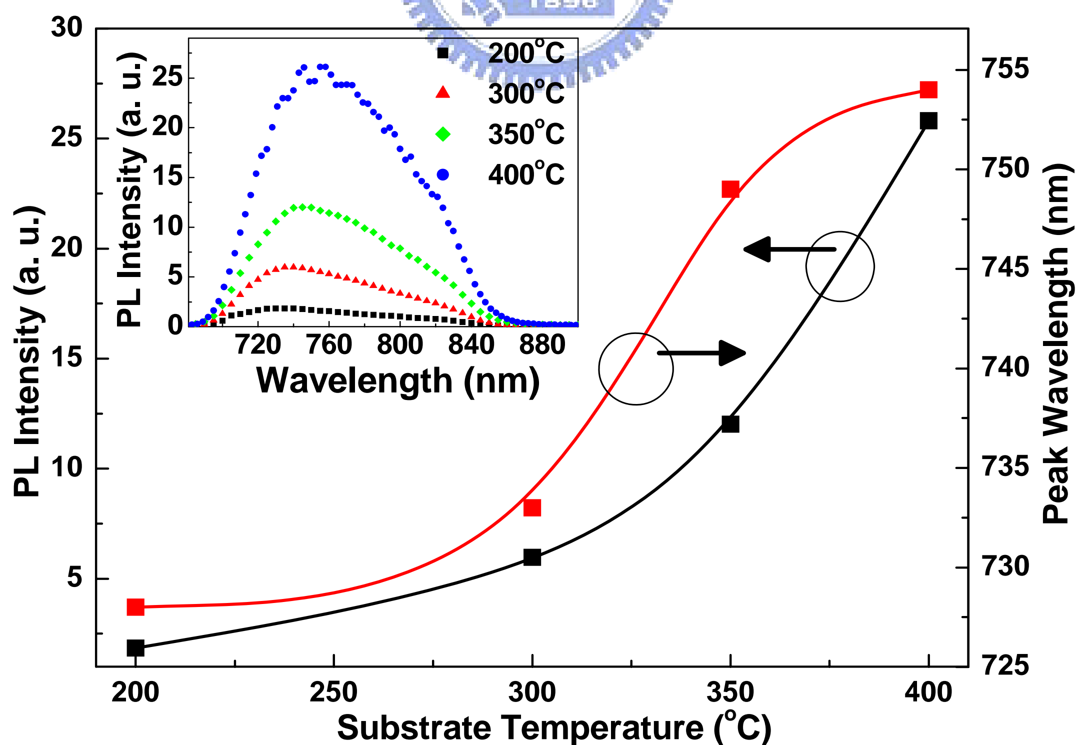


Fig. 14 PL intensity and peak wavelength as a function of substrate temperature.

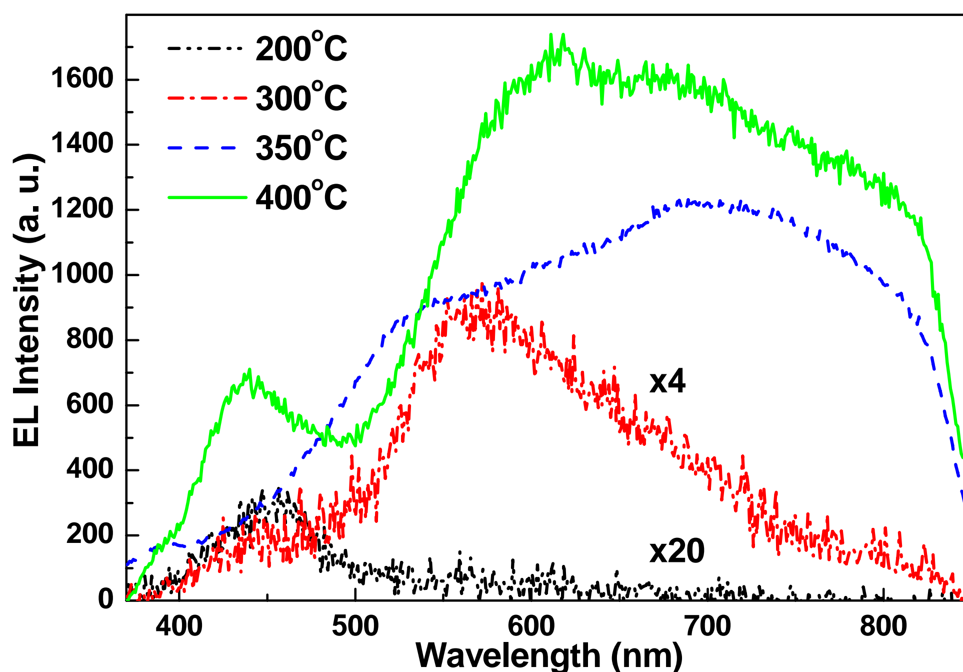


Fig. 15 EL spectra of samples prepared under different substrate temperatures.

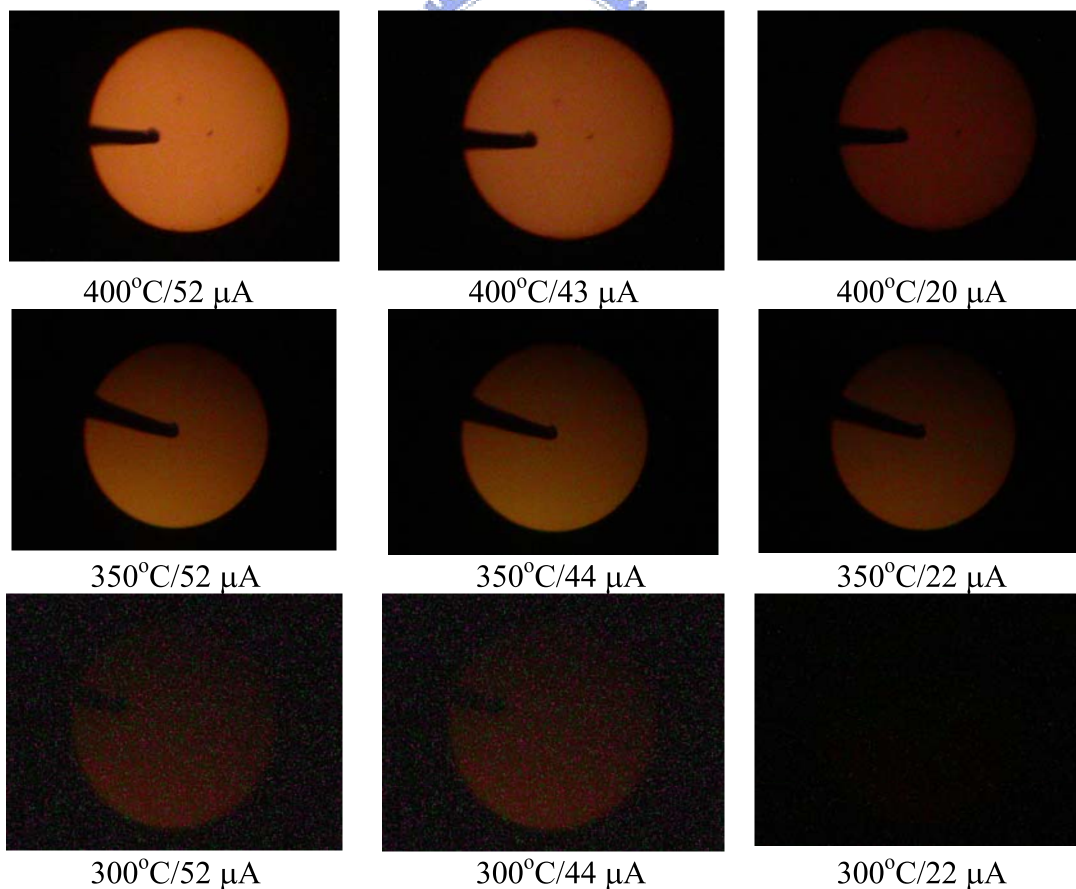


Fig. 16 EL patterns of ITO/SiOx:nc-Si/p-Si/Al MOSLED.

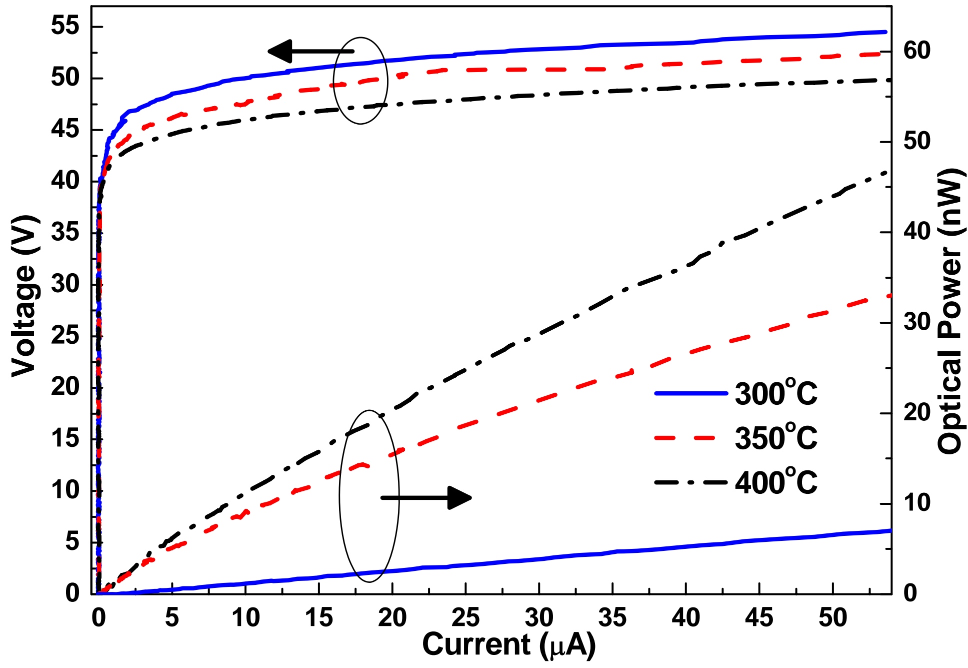


Fig. 17 I-V and P-I curves of ITO/$SiO_x$:nc-Si/p-Si/Al MOSLED.

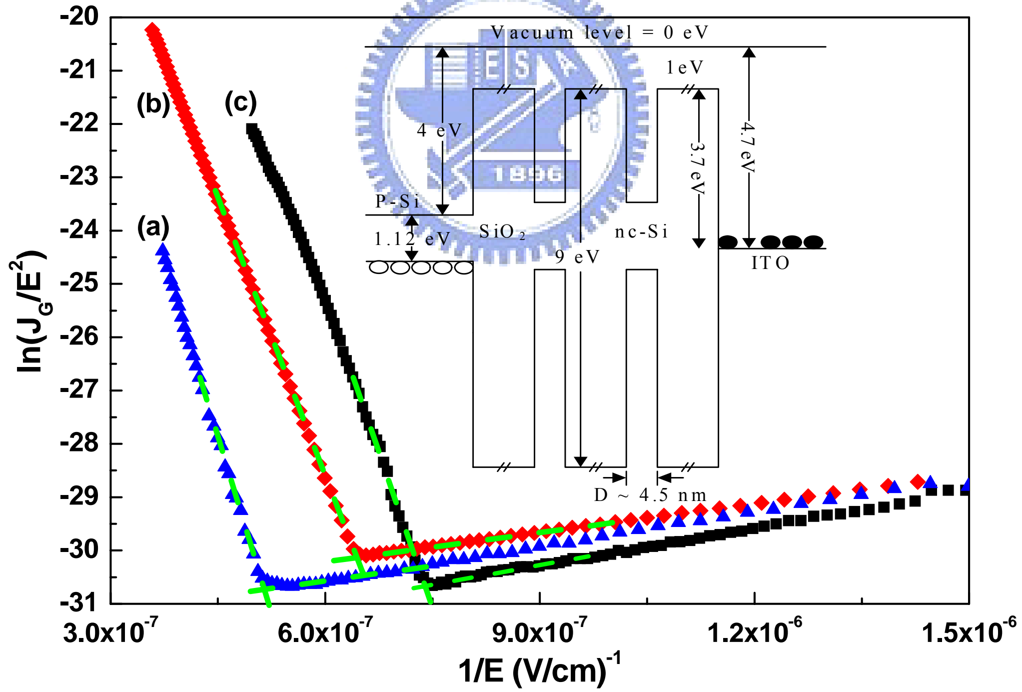


Fig. 18 Plot of $\ln(J_G/E^2)$ as a function of 1/E for three ITO/SiOx:nc-Si/p-Si/Al MOSLEDs with their SiOx grown at (a) 300, (b) 350 and (c) 400°C. Inset: Band structure of ITO/$SiO_x$:nc-Si/p-Si MOSLED.

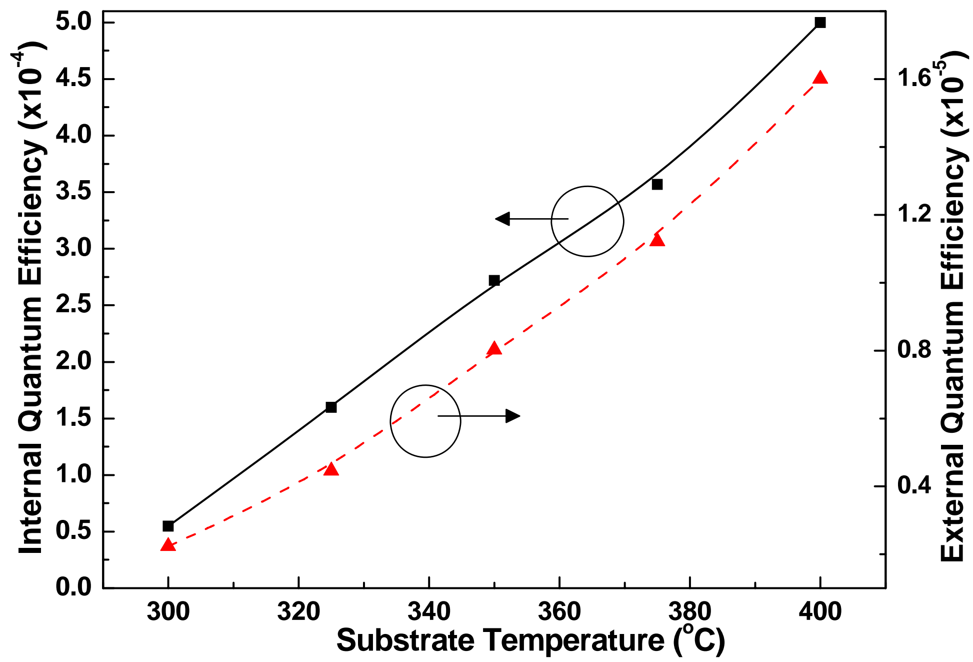


Fig. 19 Internal and external quantum efficiencies as a function of substrate temperature.

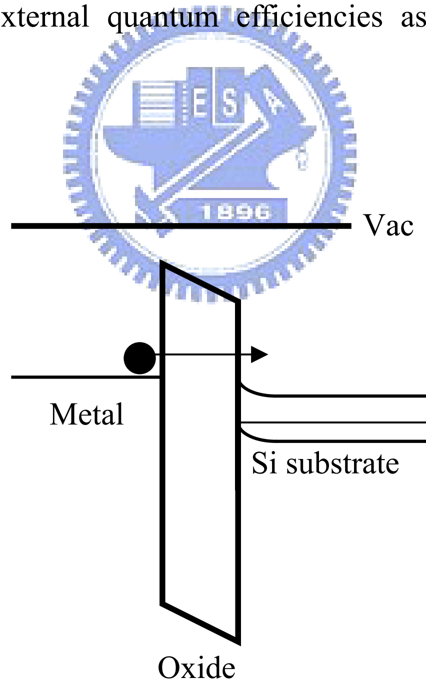


Fig. 20 Direct tunneling mechanism of MOS diode

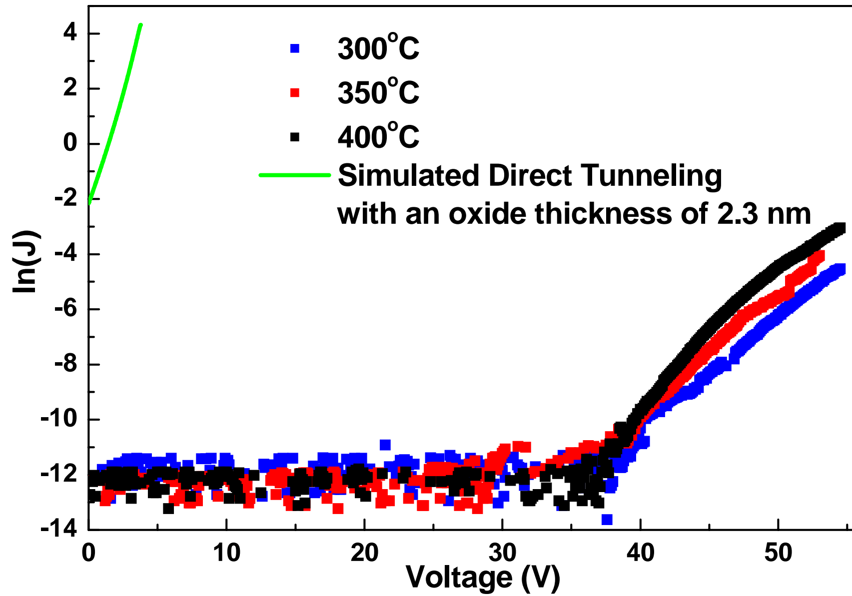


Fig. 21 Plot of ln(J) as a function of voltage for three different ITO/$SiO_x$:nc-Si/p-Si/Al MOSLEDs with their $SiO_x$ grown at 300, 350 and 400°C and a simulated direct tunneling current (solid line).

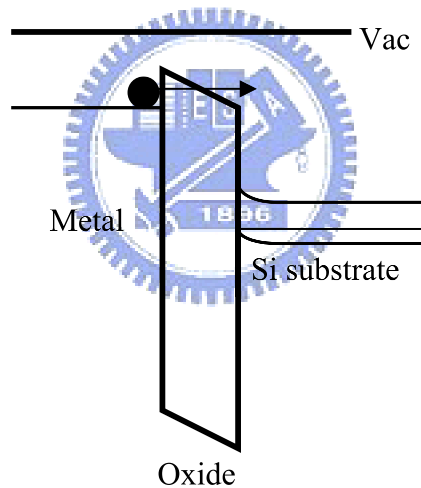


Fig. 22 Fowler-Nordheim tunneling mechanism of MOS diode

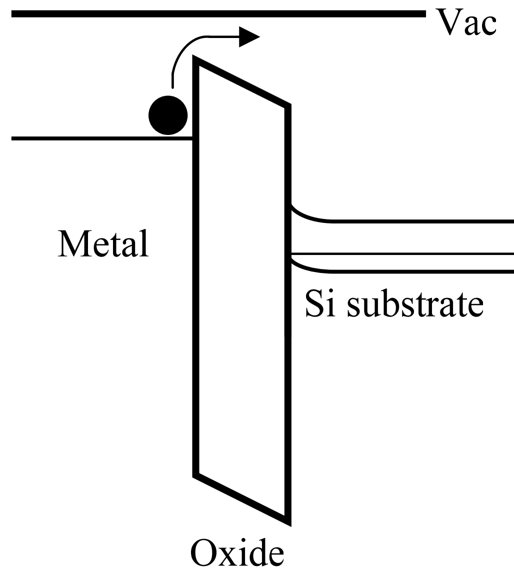


Fig. 23 Thermionic emission tunneling mechanism of MOS diode

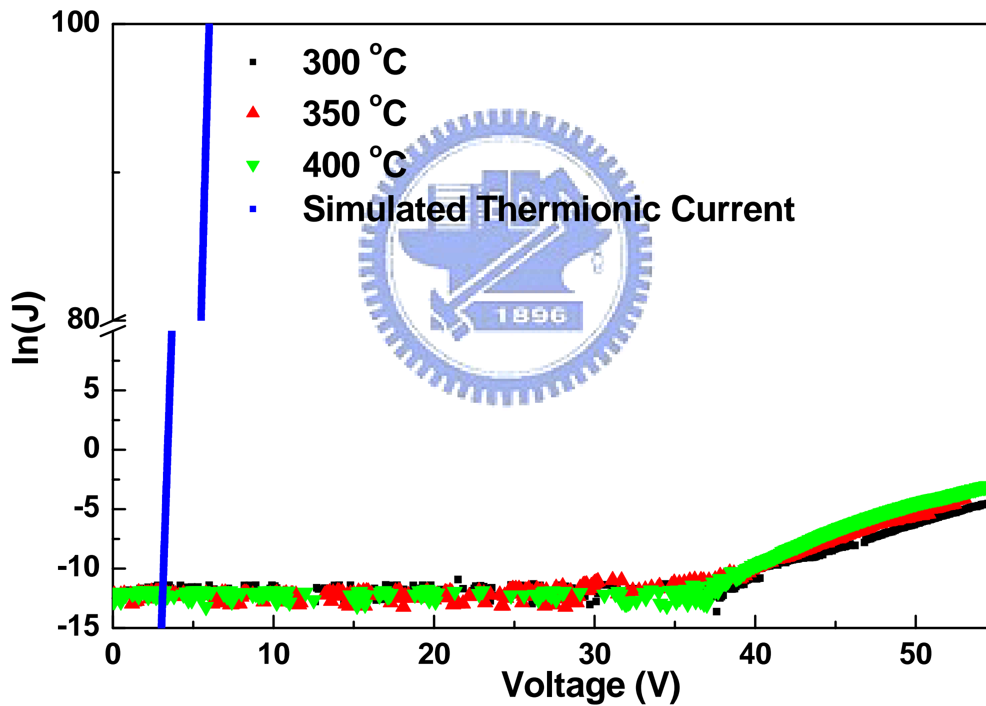


Fig. 24 Plot of ln(J) as a function of voltage for three ITO/$SiO_x$:nc-Si/p-Si/Al MOSLEDs with their $SiO_x$ grown at 300, 350 and 400°C and a simulated thermionic current.

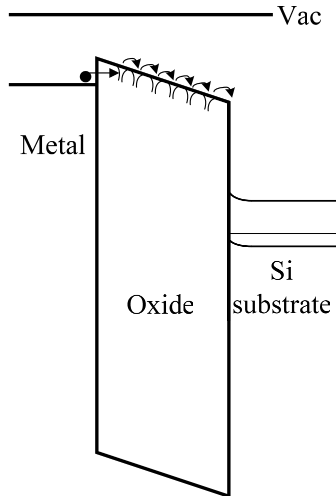


Fig. 25 Poole-Frenkel tunneling mechanism of MOS diode

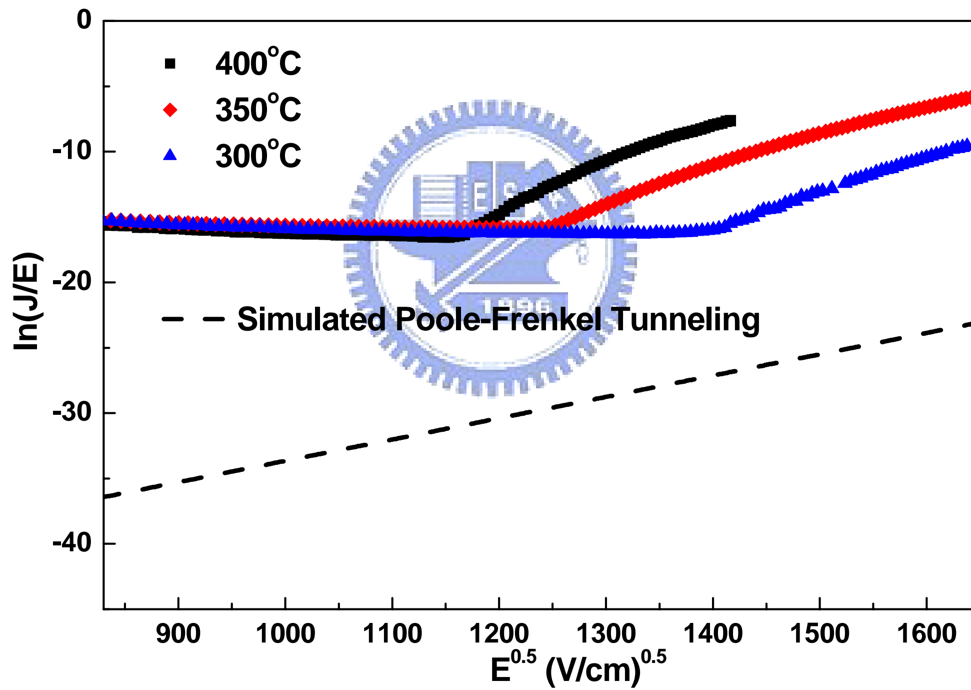


Fig. 26 Plot of ln(J/E) as a function of $E^{0.5}$ for three ITO/$SiO_x$:nc-Si/p-Si/Al MOSLEDs with their $SiO_x$ grown at 300, 350 and 400°C and a simulated Poole Frankel tunneling current.

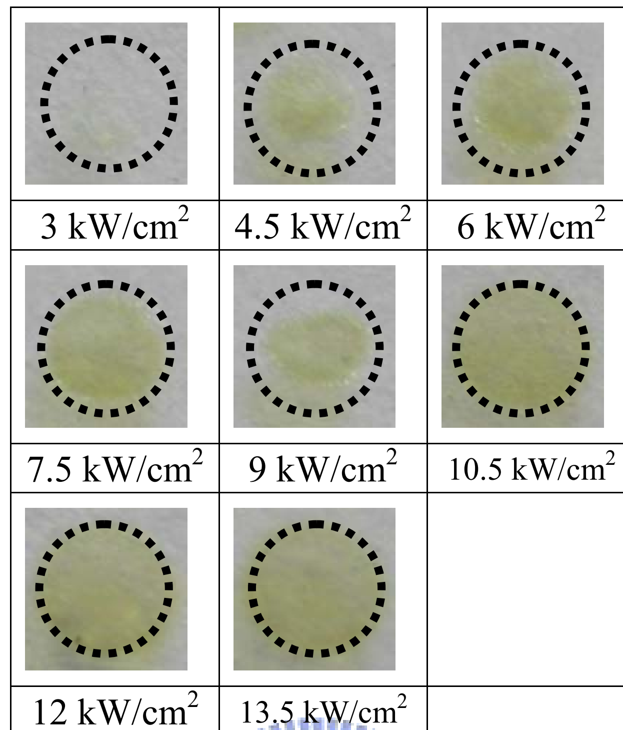


Fig. 27 Images of $SiO_{1.25}$ film after $CO_2$ laser annealing at $P_{laser}$ increasing from 3 to 13.5 kW/cm$^2$.

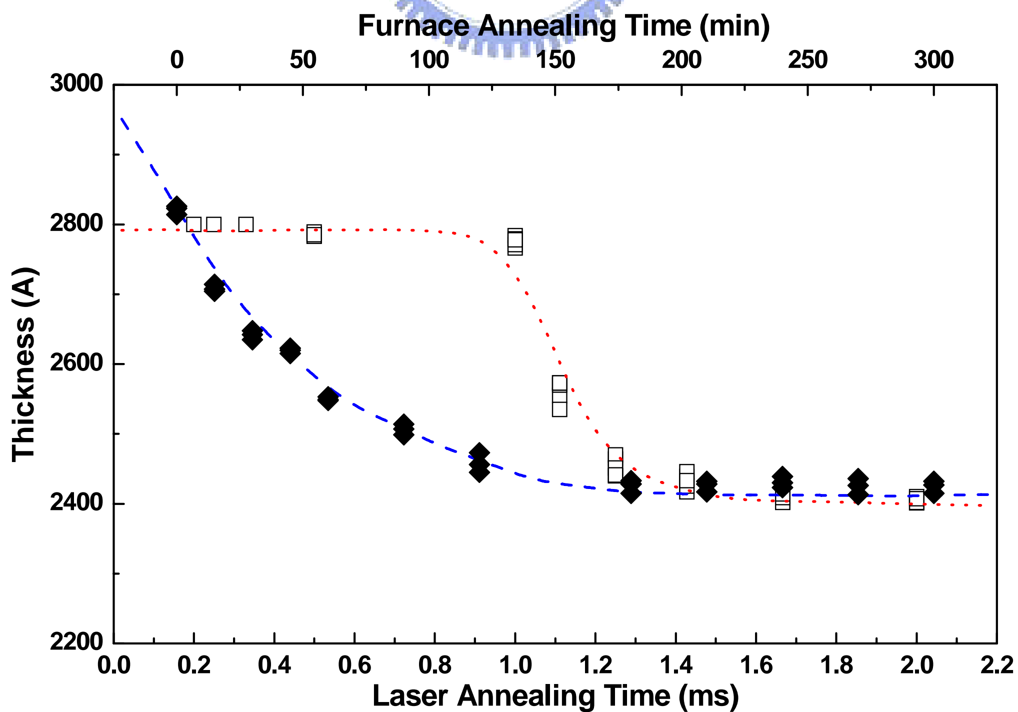


Fig. 28 The thicknesses of annealed $SiO_{1.25}$ films as a function of annealing time.

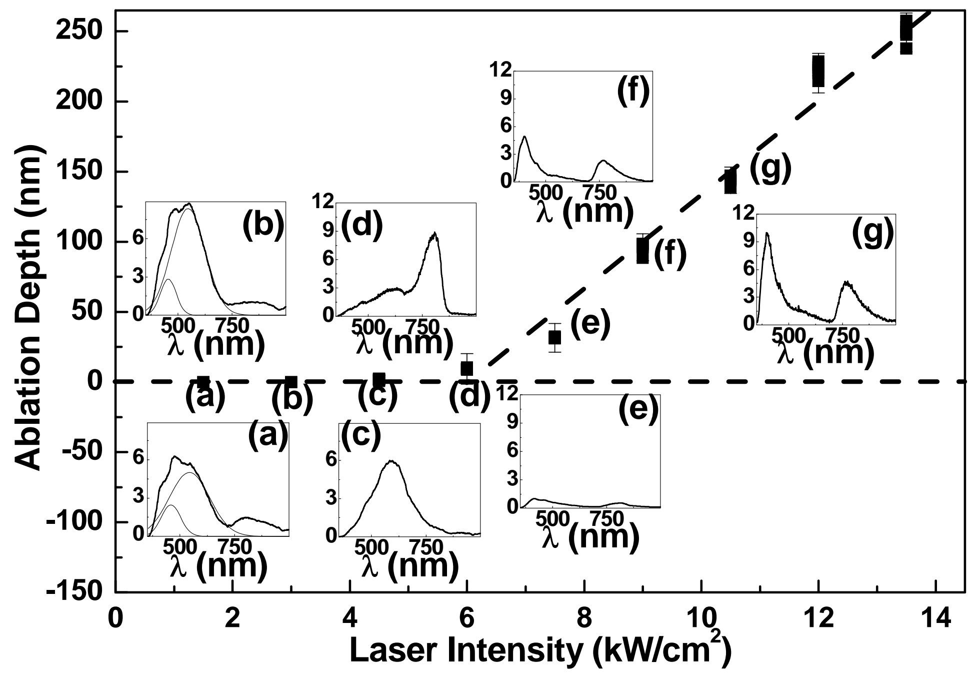


Fig. 29 Ablation thickness of $SiO_x$ as a function of $P_{laser}$. Inset: PL spectra of $CO_2$ laser annealed $SiO_{1.25}$ films at $P_{laser}$ = (a)1.5 (b)3 (c)4.5 (d)6 (e)7.5 (f)9 (g)10.5 kW/cm$^2$.

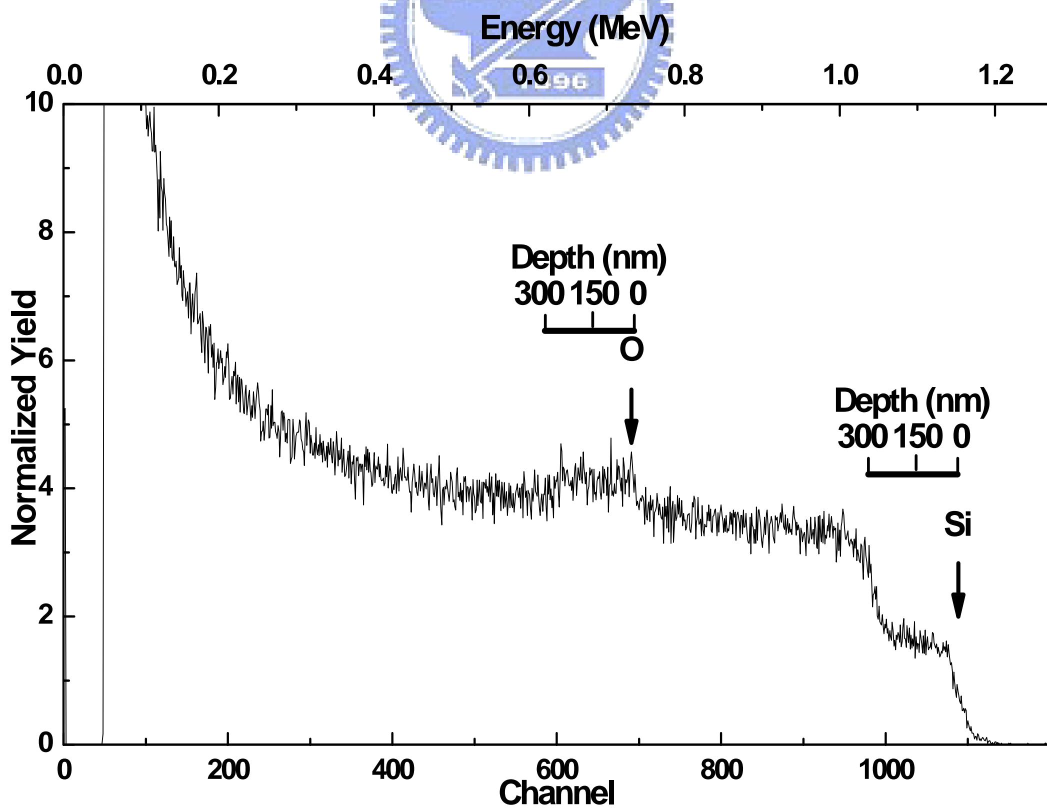


Fig. 30 RBS spectrum of the as-grown $SiO_{1.25}$ film on a Si substrate.

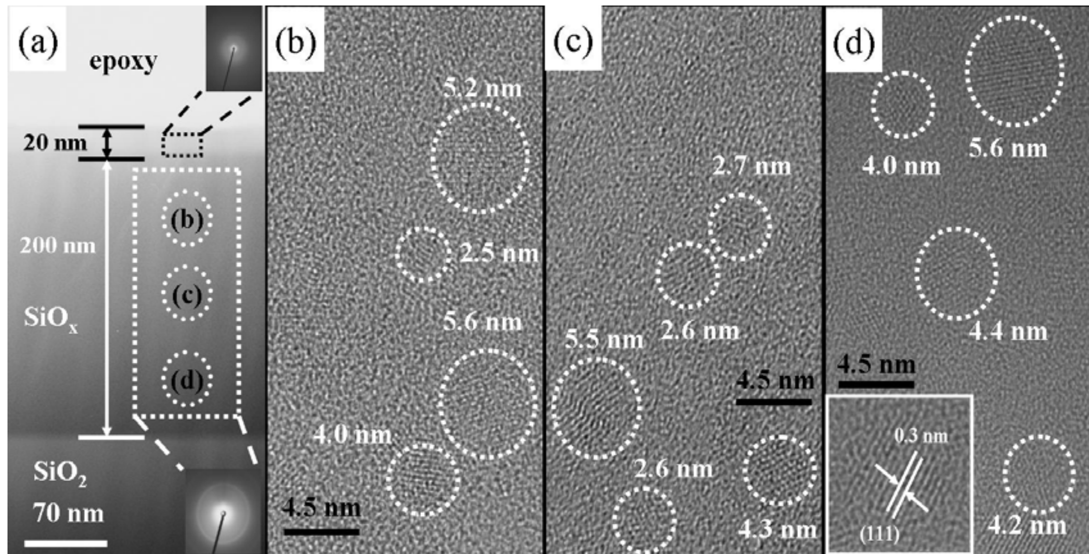


Fig. 31 Cross-sectional HRTEM images of $SiO_x$ $CO_2$-laser-annealed at $P_{laser}$ = 6 kW/$cm^2$. Inset: the electron diffraction pattern (lower right) of a (111)-plane Si nanocrystal (lower left).

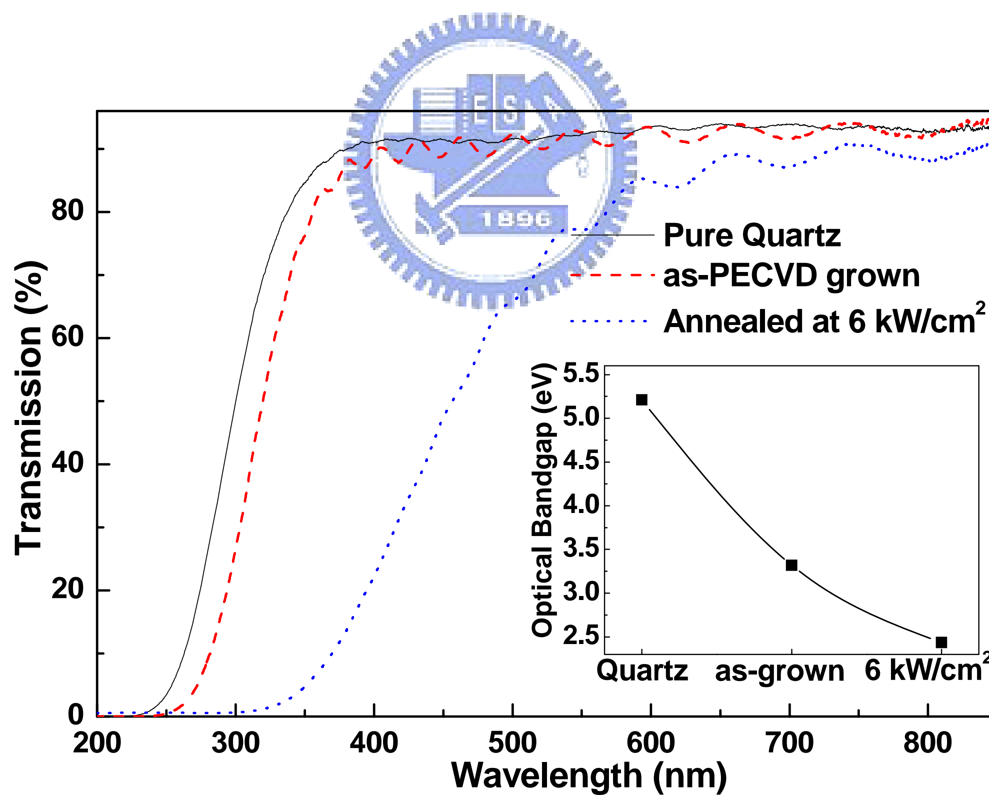


Fig. 32 Transmission spectra of Quartz, as-PECVD grown $SiO_{1.25}$ film and the $CO_2$ laser annealed $SiO_{1.25}$ film at $P_{laser}$ = 6 kW/$cm^2$.

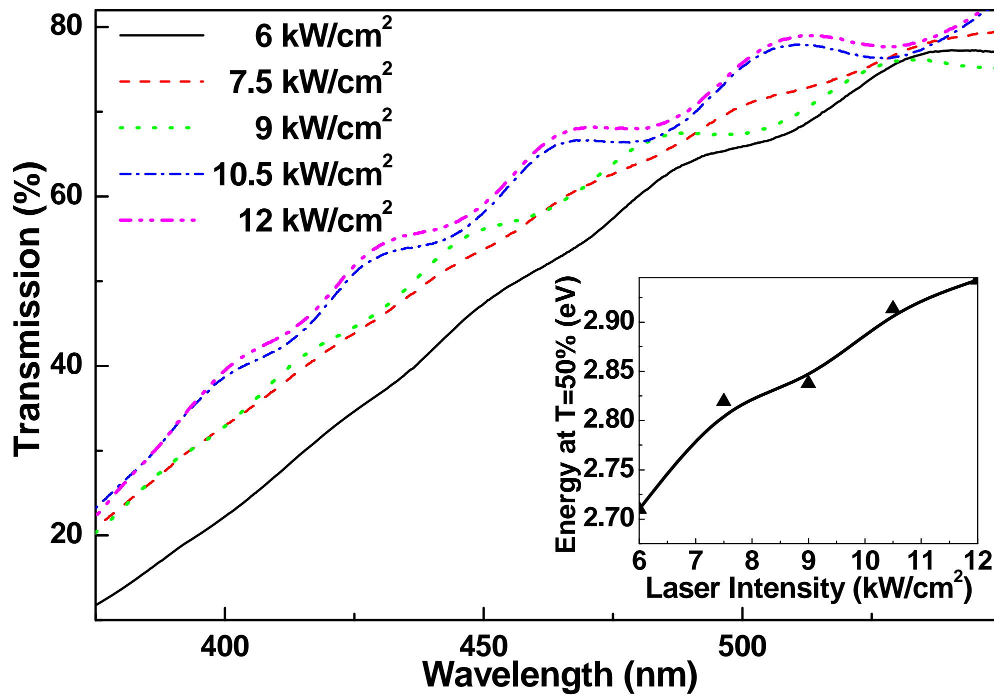


1896

Fig. 33 Transmission spectra of $CO_2$ laser annealed $SiO_{1.25}$ films at $P_{laser}$ increasing from 6 to 12 kW/cm$^2$.

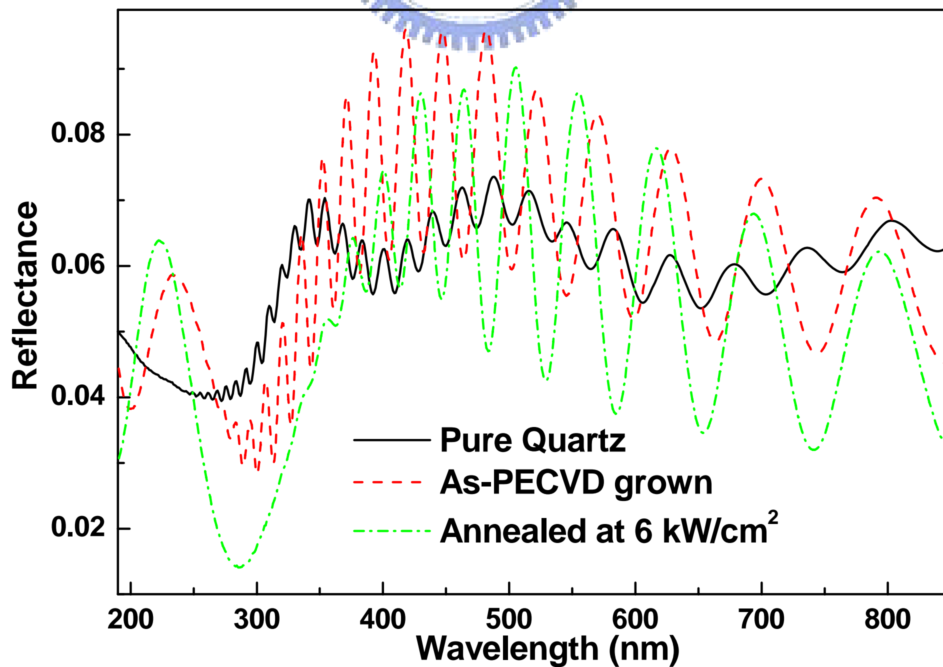


Fig. 34 Reflectance spectra of the quartz substrate, as-PECVD grown $SiO_{1.25}$ film and the $CO_2$ laser annealed $SiO_{1.25}$ film at $P_{laser}$ = 6 kW/cm$^2$

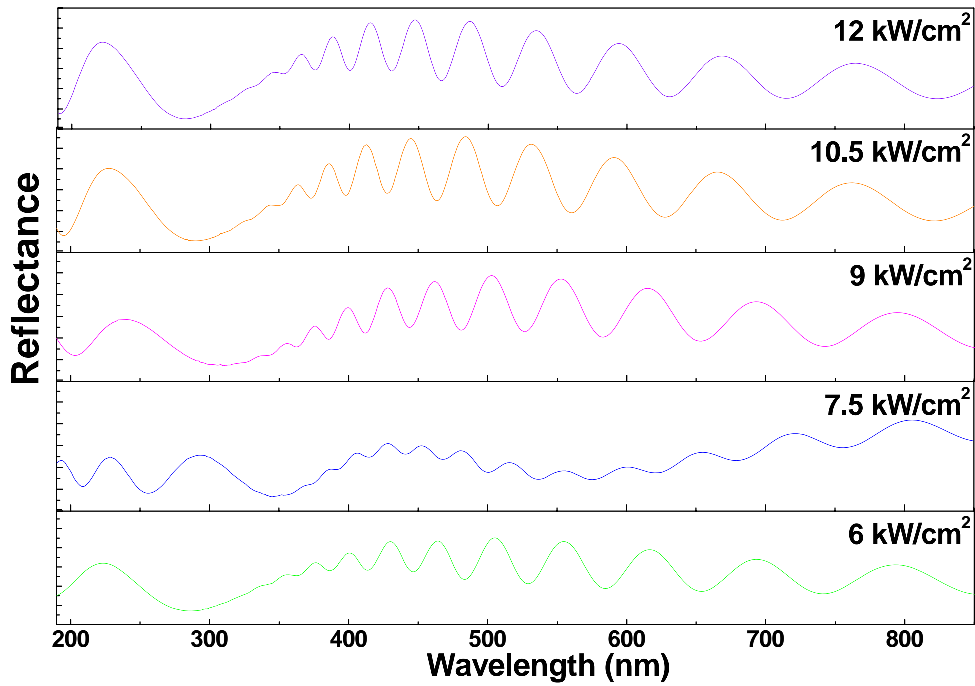


Fig. 35 Reflectance spectra of $CO_2$ laser annealed $SiO_{1.25}$ films at $P_{laser}$ increasing from 6 to 12 kW/cm$^2$.

1896

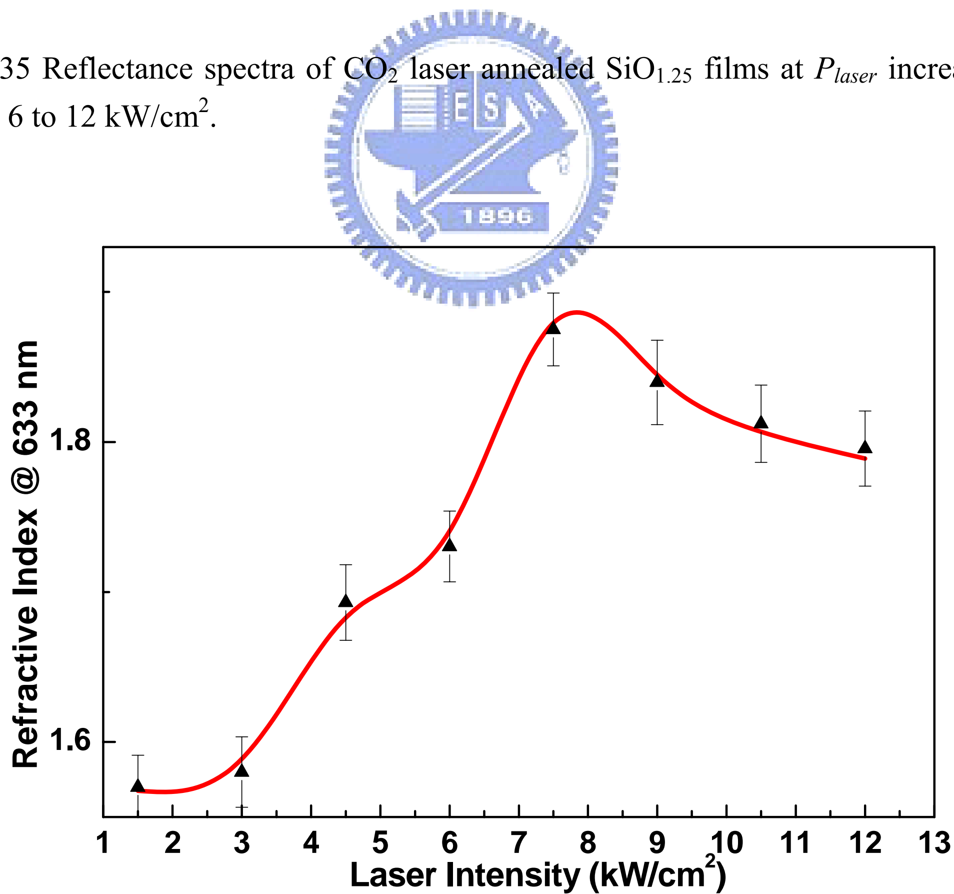


Fig. 36 Refractive index of $CO_2$ laser annealed $SiO_{1.25}$ film as a function of $P_{laser}$.

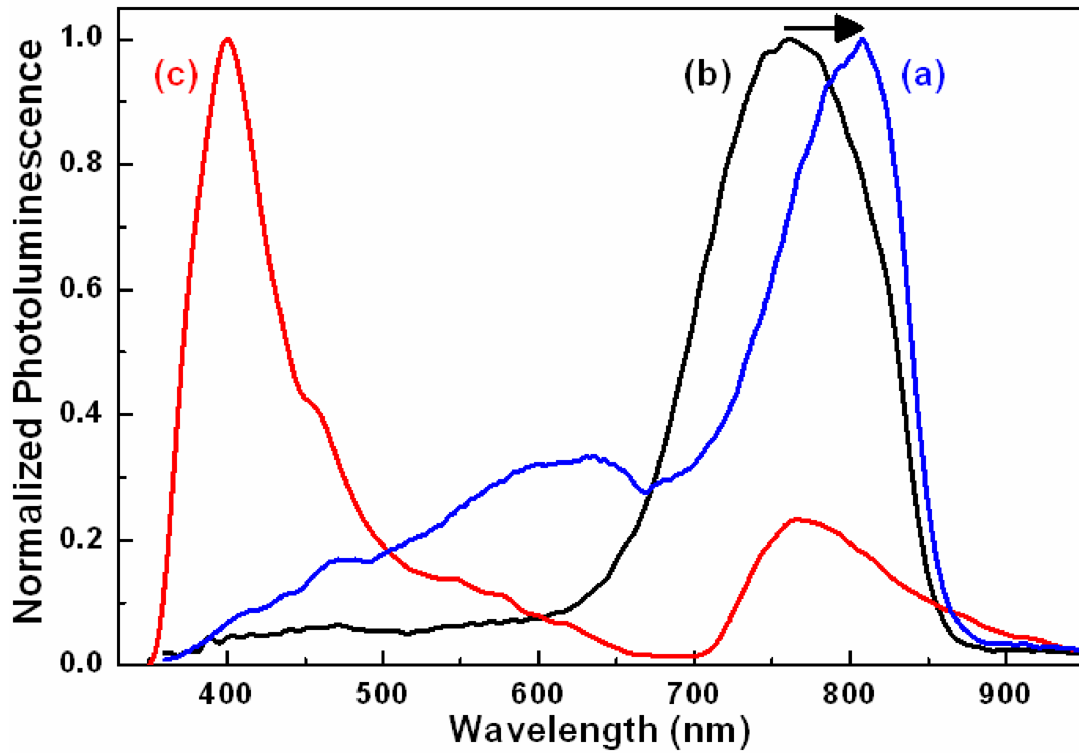


Fig. 37 PL spectra of $CO_2$ laser annealed $SiO_x$ at (a) 6 kW/cm$^2$, (b) furnace-annealing at 1100$^o$C for 30 min and $CO_2$ laser annealed $SiO_x$ at (c) 12 kW/cm$^2$.

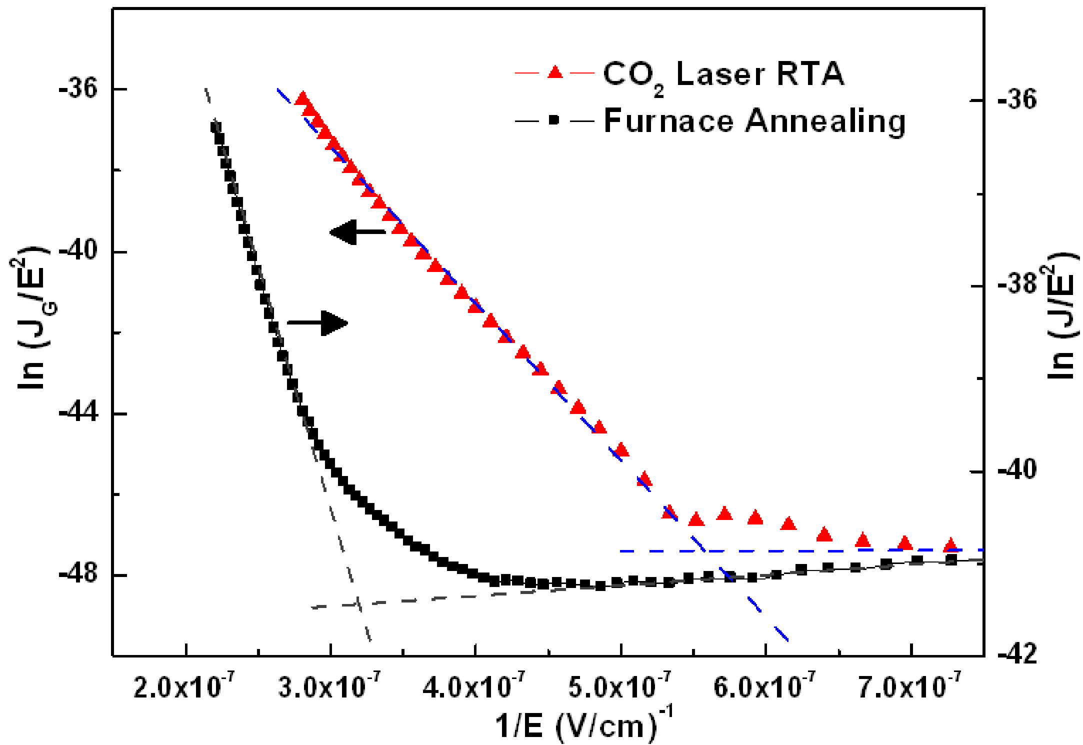


Fig. 38 Plot of $\ln(J_G/E^2)$ as a function of 1/E for $CO_2$ laser-annealed and furnace-annealed MOSLEDs.

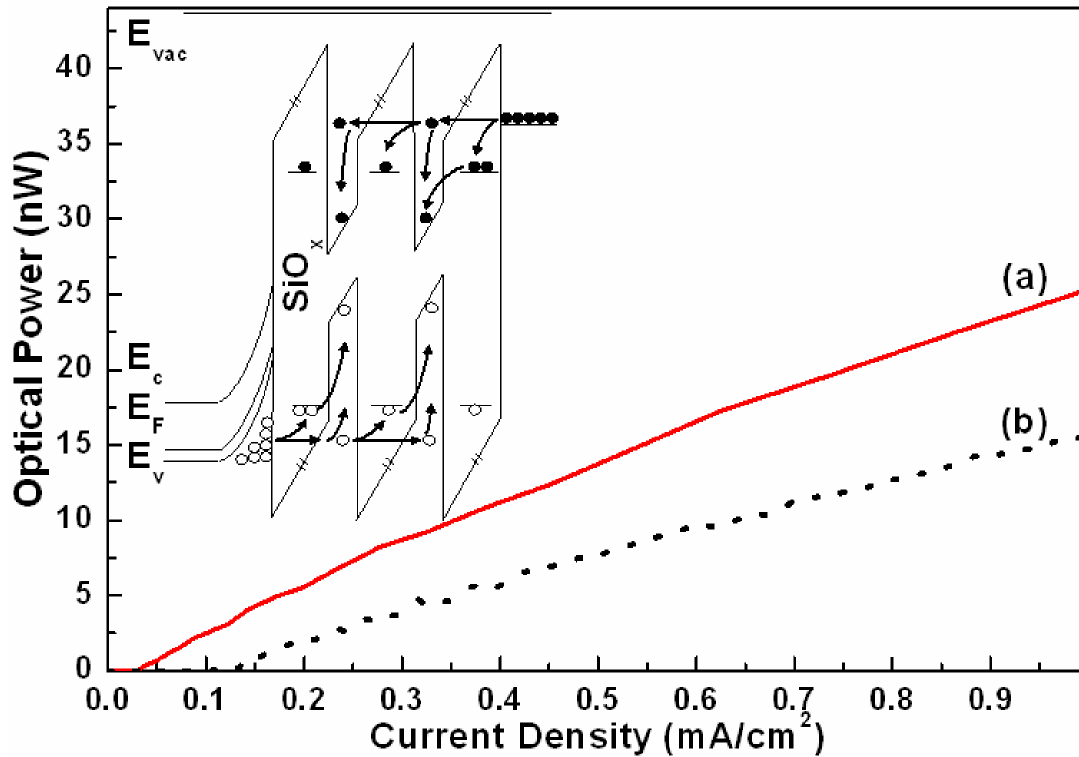


Fig. 39 P-I curves of (a) ITO/ $CO_2$ laser RTA $SiO_x$ /p-Si/Al and (b) ITO/ furnace-annealed $SiO_x$ /p-Si/Al MOSLEDs. Inset: Energy band diagram of a highly forward biased ITO/ $CO_2$ laser RTA $SiO_x$ /p-Si/Al MOSLED.

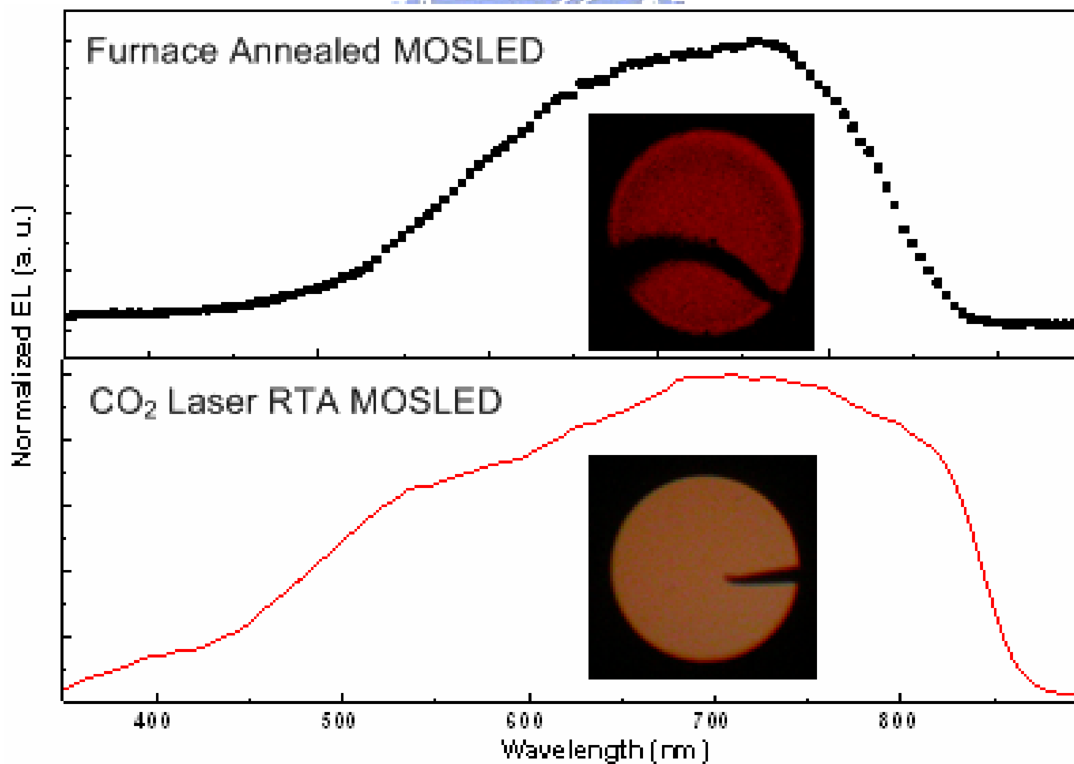


Fig. 40 EL spectra of MOSLEDs made by $CO_2$ laser RTA (lower) and furnace-annealed (upper) $SiO_x$. Inset: EL patterns of $CO_2$ laser RTA (lower) and furnace-annealed (upper) MOSLEDs